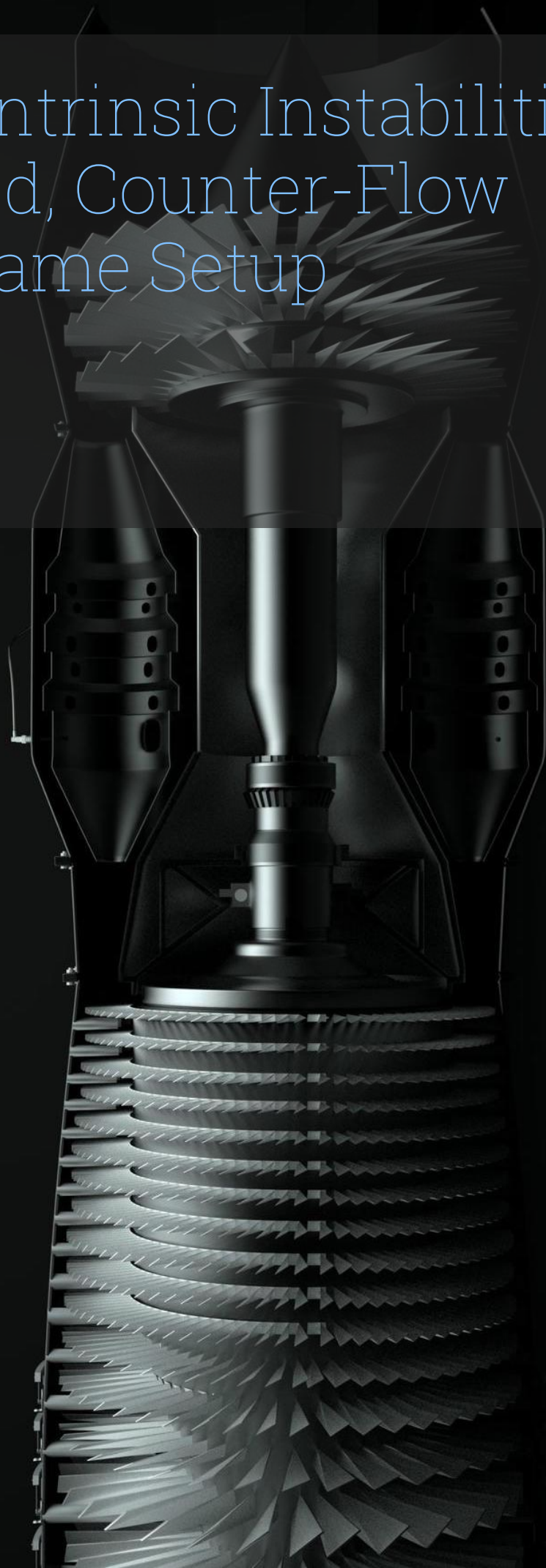


Analysis of Intrinsic Instabilities in a Premixed, Counter-Flow Hydrogen Flame Setup

Thesis Report

Ribhav Khanduja



Analysis of Intrinsic Instabilities in a Premixed, Counter-Flow Hydrogen Flame Setup

Thesis Report

by

Ribhav Khanduja

Student Number

5337887

in partial fulfilment of the requirements for the degree of

Master of Science
in Aerospace Engineering

at the Delft University of Technology,
to be defended publicly on October 17, 2024.

Supervisor: Dr. Ivan Langella
Project Duration: February, 2023 - October, 2024
Faculty: Faculty of Aerospace Engineering, Delft
Track: Flight Performance and Propulsion
Profile: Flight Performance

Preface

It is an overwhelming feeling to witness this thesis mark the culmination of my master's journey at TU Delft. The past couple of years have been both intense and transformative, filled with numerous challenges and profound growth. Reflecting on this experience, I am filled with gratitude for how TU Delft has shaped my academic and personal development.

I would like to extend my heartfelt appreciation to my supervisor, Dr. Ivan Langella. His invaluable guidance throughout every phase of this thesis, from the initial learning stages to the final results, has been instrumental in my progress. Additionally, I am deeply grateful to Alessandro, whose unwavering support and insights into my methodology and results have greatly enriched my work. His availability and willingness to assist me whenever needed made a significant difference in my journey.

I also wish to thank my committee members, Chair Professor Dr. Fulvio Scarano and Dr. Francesca De Domenico, for taking the time to read and evaluate my thesis.

My thesis colleagues, Pranav and Vijit, have been tremendous friends and collaborators throughout this process. Their encouragement and camaraderie helped me navigate the challenges of this thesis.

I owe a special debt of gratitude to my parents for their financial support and encouragement throughout my studies. My sister, Nishna, and my closest friends have also been vital pillars of support during this journey. Lastly, I would like to acknowledge my extended family for their unwavering belief in me.

This thesis is not just a culmination of my academic efforts but a testament to the incredible support network that has guided me along the way.

जय गुरुदेव
Ribhav Khanduja
Delft, October 2024

Abstract

This study investigated the effect of tangential strain on the stability of perturbed laminar lean premixed hydrogen flames in a counterflow reactants-to-products configuration. Laminar premixed flames are highly susceptible to intrinsic instabilities, including hydrodynamic and thermodiffusive instabilities, which can cause perturbations in the flame front to grow. However, the impact of tangential strain, introduced by velocity gradients along the flame front in a counterflow setup, had not been fully explored in the context of flame stability. The present work bridged this gap by combining the counterflow setup used in previous studies of NO_x reduction with the perturbation analysis commonly employed in flame stability research.

Direct Numerical Simulations were performed to study the behaviour of sinusoidal perturbations imposed on the flame front, focusing on the growth rates of these perturbations under two different strain rates (2000 s⁻¹ and 4000 s⁻¹). The results indicated that the tangential strain improved the stability of the flame front, as the strain rate led to a reduction in both the maximum observed growth rate and the growth rate after the perturbation reached its peak. The growth rates observed were in the non-linear regime, characterised by continual variation over time. At higher strain rates, the flame front stabilised more quickly, suggesting a strong correlation between strain rate and perturbation growth dynamics. The strain-induced velocity gradients displaced the flame front, reducing its effective curvature and wavelength, further contributing to the stabilisation process.

In addition to the strain rate, the study investigated the effects of varying the amplitude and wavelength of initial perturbations. It was found that the amplitude of the initial perturbation had little impact on the maximum growth rate, but variations in the initial wavelength significantly influenced both the growth dynamics and the maximum growth rate of the perturbations.

Overall, the results provided a comprehensive understanding of how tangential strain affected flame stability and highlighted the importance of wavelength variations in determining perturbation growth rates. These findings provide insights into potential strategies to improve flame stability in practical combustion systems aimed at reducing emissions, such as in lean hydrogen combustion.

Contents

Preface	i
Abstract	ii
Nomenclature	vi
1 Introduction	1
1.1 The Role of Climate Change in Energy Transition	1
1.2 Variation in Physical & Chemical Properties of Hydrogen	2
1.3 Challenges Posed by the Combustion of Hydrogen	3
1.3.1 Higher Propensity for Flashback	3
1.3.2 Higher NO _x Emissions	4
1.4 Strategies for Emission Control	5
1.5 Combustor Designs for Hydrogen Gas Turbines	6
1.5.1 Diffusion Flame Combustor Designs	6
1.5.2 Premixed Combustor Designs	7
1.6 Understanding Turbulent Combustion through Laminar Flames	8
2 Research Background	10
2.1 Markstein Number Effects	10
2.1.1 Summary	10
2.2 Intrinsic Flame Instabilities	11
2.2.1 Study	13
2.2.2 Implications for Thesis Methodology	13
2.3 Thermoacoustic Instabilities	13
2.3.1 Study	14
2.3.2 Implications for Thesis Methodology	14
2.4 Differential Diffusion Effects	14
2.4.1 Derivations and Summary	14
2.4.2 Studies	16
2.4.3 Implications for Thesis Methodology	17
2.5 Soret Effect	18
2.5.1 Summary	18
2.5.2 Studies	18
2.5.3 Implications for Thesis Methodology	18
2.6 More Numerical Simulations of Hydrogen Flames	19
2.7 NO _x Trends in Strained Hydrogen Premixed Laminar Flames	20
2.8 Intrinsic Instabilities in Premixed Hydrogen Flames	20
2.9 Identifying a Gap in the Literature	21
2.10 Research Questions	21
3 Combustion Mechanisms for Hydrogen	22
3.1 GRI-Mech 3.0 [81]	22
3.1.1 Overview	22
3.1.2 Validation Data	22

3.2	H ₂ /O ₂ Chemical Kinetic Mechanism (Li et al.) [83]	22
3.2.1	Overview	22
3.2.2	Validation Data	23
3.3	San Diego Chemical Kinetic Mechanism [85]	23
3.3.1	Overview	23
3.3.2	Validation Data	23
3.4	Capurso et al. Chemical Kinetic Mechanism [87]	23
3.4.1	Overview	23
3.4.2	Validation Data	23
3.5	Implications for Thesis Methodology	24
4	Methodology	25
4.1	Governing Equations	25
4.2	Solver Parameters	26
4.3	Combustion Model	26
4.4	Strained Counterflow Reactants-to-Products Configuration	27
4.5	Navier Stokes Characteristic Boundary Conditions (NSCBC)	30
4.6	Imposing Harmonic Perturbations to the Flame Front	33
4.7	Flame Front Tracking	35
5	Results and Analysis	38
5.1	Mesh Sensitivity Analysis	38
5.2	Flame-Front Evolution for Perturbed Simulations at 4000s ⁻¹	40
5.3	Flame-Front Evolution for Perturbed Simulations at 2000s ⁻¹	43
5.4	Growth Rates for Perturbed Simulations at 4000s ⁻¹	45
5.5	Growth Rates for Perturbed Simulations at 2000s ⁻¹	47
5.6	Comparisons to Results from Berger et al. [51]	50
6	Conclusions and Recommendations	52
6.1	Conclusions	52
6.1.1	Effects of tangential strain on the stability of perturbed laminar lean premixed hydrogen flames	52
6.1.2	Effects of varying the amplitudes and wavelengths of the initial perturbations imposed on strained laminar lean premixed hydrogen flame fronts	52
6.1.3	Presence of thermoacoustic instabilities and the influence of strain rate	53
6.2	Recommendations	53
6.2.1	Flame-Front Tracking and Wavelength Determination	53
6.2.2	Perturbation of All Fields except for the Velocity Field	53
A	Map File Modifying Code	54
	References	57

List of Figures

1.1	The variation in production of pollutants as a function of temperature and equivalence ratio (ϕ) [30]	4
1.2	Simplified pathways for NO_x formation in hydrogen combustion [35] (red for thermal NO, green for NNH-NO, black for NNH-HNO-NO, and blue for N_2O -NO)	5
1.3	GE10 Diffusive Flame Combustor from Cocchi et al. [46]	7
1.4	Turbtec T100 Combustor [47]	7
1.5	TG50 DLN Combustor Prototype [48]	8
1.6	Conventional Combustor vs New Combustor Prototype from Inoue et al. [49]	8
2.1	The Markstein number (\mathcal{M}) for various fuel-air flames, varying with equivalence ratio (ϕ) [55]	11
2.2	Diagram depicting Darrieus–Landau (hydrodynamic) instability [57]	12
4.1	Counter-flow Reactants-to-Products Setup from Porcarelli et al. [35]	28
4.2	Preferential Diffusion due to Uneven Mesh Size	29
4.3	Modified Setup of Porcarelli et al. [35] in ConvergeCFD	30
4.4	Pressure Field Fluctuating at Consecutive Time Steps	31
4.5	Perturbing the Flame Front	34
4.6	Tracking of the Central Peak and Adjacent Trough	35
4.7	Streamlines Displaying the Tangential Velocity Gradients at the Flame Front	36
5.1	Normalised Growth Rate vs Normalised Solution Time	38
5.2	Normalised Wave Number vs Normalised Solution Time	39
5.3	Evolution of the Flame-Front with Time (Case 1)	40
5.4	Evolution of the Flame Front with Time (Case 2)	41
5.5	Evolution of the Flame Front with Time (Case 3)	41
5.6	Evolution of the Flame Front with Time (Case 4)	42
5.7	Evolution of the Flame-Front with Time (Case 5)	43
5.8	Evolution of the Flame Front with Time (Case 6)	43
5.9	Evolution of the Flame Front with Time (Case 7)	44
5.10	Evolution of the Flame Front with Time (Case 8)	44
5.11	Normalised Growth Rate vs Normalised Solution Time	45
5.12	Normalised Wave Number vs Normalised Solution Time	46
5.13	Normalised Growth Rate vs Normalised Wave Number	46
5.14	Normalised Growth Rate vs Normalised Solution Time	47
5.15	Normalised Wave Number vs Normalised Solution Time	48
5.16	Normalised Growth Rate vs Normalised Wave Number	49
5.17	Normalised Growth Rate vs Normalised Wave Number	50
5.18	Normalised Growth Rate vs Normalised Solution Time	51

Nomenclature

Abbreviations

Abbreviation	Definition
1D	One Dimension
2D	Two Dimension
3D	Three Dimension
AFR	Air-to-Fuel Ratio
CFL	Courant–Friedrichs–Lewy
CFD	Computational Fluid Dynamics
DNS	Direct Numerical Simulations
DL	Darrieus-Landau
EGR	Exhaust Gas Recirculation
ER	Equivalence Ratio
GHGs	Greenhouse Gases
Gt	Gigatons
HFCs	Hydrofluorocarbons
ICAO	International Civil Aviation Organisation
K	Kelvin
LES	Large Eddy Simulations
LHV	Lower Heating Value
LODI	Local One-Dimensional Incompressible
mm	Millimeters
NSCBC	Navier-Stokes Characteristic Boundary Conditions
Pa	Pascals
PDFs	Probability Density Functions
PFCs	Perfluorocarbons
PISO	Pressure Implicit with Splitting of Operator
ppm	Parts per million
SCR	Selective Catalytic Reduction
TCRE	Transient Climate Response to cumulative carbon Emissions
TD	Thermodiffusive
UHCs	Unburned Hydrocarbons

Symbols

Symbol	Definition	Unit
a	Applied (local) strain rate	[1/s]
A	Amplitude	[-]
A_0	Initial Amplitude	[-]
C_{H_2}	Hydrogen Progress Variable	[-]
D	Mass Diffusivity	[m ² /s]
$\dot{\omega}_F$	Fuel Reaction Rate	[kg/m ³ /s]
k	Wavenumber	[1/m]
K	Stretch	[1/s]
l_F	Laminar Flame Thickness (Stretched)	[m]
$l_{F,u}$	Unstretched Laminar Flame Thickness	[m]
Le	Lewis number	[-]
Le_{eff}	Effective Lewis number	[-]
p	Pressure	[Pa]
Re	Reynolds Number	[-]
S_c	Flame Consumption Speed	[m/s]
t	Time	[s]
T	Temperature	[K]
T_b	Burnt Gas Temperature	[K]
T_u	Unburnt Gas Temperature	[K]
u_r	Inlet Reactants Velocity	[m/s]
u_p	Inlet Products Velocity	[m/s]
u, v, w	Velocity Components	[m/s]
x	X location	[m]
y	Y location	[m]
Y	Mass Fraction	[-]
CH_4	Methane	[-]
CO	Carbon Monoxide	[-]
CO_2	Carbon Dioxide	[-]
H	Hydrogen Radical	[-]
H_2	Hydrogen	[-]
H_2O	Water	[-]
N_2O	Nitrous Oxide	[-]
NNH	Nitrogen Hydride	[-]
NO_x	Nitrogen Oxides	[-]
Y_{H_2}	Hydrogen Mass Fraction	[-]
$Y_{H_2,u}$	Unburned Hydrogen Mass Fraction	[-]
α	Thermal diffusivity	[m ² /s]
λ	Wavelength	[m]
λ_0	Initial Wavelength	[m]
\mathcal{L}	Markstein length	[m]
\mathcal{M}	Markstein number	[-]
ω	Growth Rate	[1/s]
ϕ	Equivalence Ratio	[-]
ρ	Density	[kg/m ³]

Introduction

1.1. The Role of Climate Change in Energy Transition

Climate change refers to significant and prolonged alterations in temperature and weather conditions across the planet. Although natural phenomena such as variations in solar radiation and significant volcanic eruptions can play a role, the primary influence since the 19th century has been human activity. The combustion of fossil fuels, including coal, oil, and natural gas, has significantly increased the concentration of greenhouse gases (GHGs) in the atmosphere. These gases trap heat, leading to an increase in global temperatures and resulting in widespread climatic changes. This anthropogenic influence is underscored by various scientific assessments, which emphasise that human-induced emissions are now the leading factor driving climate change [1]. Examples of greenhouse gases (GHGs), ranked from most to least abundant in the atmosphere, include water vapour (H_2O), carbon dioxide (CO_2), methane (CH_4), nitrous oxide (N_2O), and fluorinated gases such as hydrofluorocarbons (HFCs) and perfluorocarbons (PFCs), among others. [2]. Although water vapour is the most abundant GHG in the atmosphere, it is said to be naturally present and its abundance is dependent on meteorological conditions outside the control of humans. However, all other GHGs are emitted by humans and are therefore of interest to control.

CO_2 emissions have increased significantly from the pre-industrial era to the present day, primarily driven by human activity. Before 1850, emissions were limited to a few million tons annually, largely due to the small global population and the use of traditional biomass fuels [3]. However, industrialisation in the 20th century, powered by coal and later by petroleum, dramatically increased energy consumption and, consequently, carbon emissions. The development of energy-intensive industries, coupled with population growth, accelerated the demand for fossil fuels, culminating in the emission of 35 billion tons of CO_2 by 2020 [4]. By 2022, global CO_2 emissions reached a record 36.4 gigatons (Gt), the highest concentration in two million years [5]. This marks a rebound from the pandemic-induced drop to 34.9 Gt in 2021 [6], driven by renewed industrial activity and energy demand, especially in countries like China, which contributed 31.1% of global emissions in 2021 [6].

The relationship between global warming and cumulative carbon emissions is quantified by the Transient Climate Response to cumulative carbon Emissions (TCRE), which shows that surface warming is nearly linearly correlated to cumulative emissions [7, 8]. Studies estimate that each Gt of carbon emitted raises the global mean surface temperature by approximately 2.15°C , although this can vary due to climate feedback mechanisms [9]. Furthermore, the contribution of carbon emissions to radiative forcing is not limited to CO_2 . Other GHGs such as CH_4 and N_2O also influence radiative forcing, with varying efficiencies and atmospheric lifetimes [10, 11]. For example, CH_4 has a much higher short-term global warming potential than CO_2 , complicating the assessment of overall radiative forcing (Alvarez et al., 2012). Aerosols, particularly black carbon (also known as soot), further affect radiative forcing by both absorbing sunlight and causing warming (positive forcing) or reflecting sunlight and causing cooling (negative forcing) [12, 13]. The net effect of aerosols is complex and regionally variable, highlighting

the need to consider both direct and indirect impacts on radiative forcing [14].

As human activity continues to increase the levels of CO₂, CH₄, and other GHGs, the planet faces unprecedented environmental, economic and social impacts. Global warming, rising sea levels, extreme weather events, and loss of biodiversity are some of the direct consequences of climate change. To combat these direct consequences, governments and regulatory agencies worldwide are striving to reduce emissions across various industries to promote a greener and more sustainable planet. In the aviation sector, for instance, climate goals are established primarily by the International Civil Aviation Organisation (ICAO), which has set a target to achieve net zero CO₂ emissions from aviation by 2050 [15]. These ambitious goals have sparked a global shift in energy strategies, with industries looking to alternative, low-carbon fuel sources as part of a broader effort to combat climate change.

Hydrogen, as a potential clean energy source, plays a pivotal role in this transition. Its combustion, which mainly produces water as a by-product and does not emit carbon dioxide [16], makes it an attractive alternative to traditional fossil fuels. Furthermore, hydrogen also offers a solution to the problem of pollutants such as soot and carbon monoxide that are associated with hydrocarbon-based fuels. However, the production and use of hydrogen must be carefully managed to ensure that it contributes meaningfully to the emission reduction goals. Hydrogen can be generated in several ways, including from natural gas using steam methane reformation (grey hydrogen), from fossil fuels with carbon capture and storage (blue hydrogen), or from renewable energy sources through water electrolysis (green hydrogen) [17]. The latter, green hydrogen, has the most potential to align with climate objectives, as it ensures that the entire hydrogen life cycle remains low in carbon emissions.

The transition toward hydrogen and other renewable fuels is driven by the urgent need to decarbonise sectors that have been resistant to change, such as heavy industry, aviation, and maritime transport. These sectors face unique challenges in reducing emissions, as the energy densities required for their operations are difficult to meet with traditional renewables like wind and solar. In 2019, the aviation sector alone accounted for 2.5% of the global CO₂ emissions from fossil fuel sources [18]. However, when considering its total contribution to global warming, including non-CO₂ effects such as contrails, aviation has an approximate 3.5% contribution to the effective radiative forcing [19] and has contributed around 4% of the increase in global temperature since preindustrial times [20]. Hydrogen, with its high energy density and flexibility, offers a viable solution, particularly in combustion systems, where it can serve as a cleaner alternative to conventional hydrocarbon fuels.

Nonetheless, the energy transition is not without its complexities. Although hydrogen combustion eliminates CO₂ emissions, it can still lead to the production of nitrogen oxides (NO_x) in various layers of the atmosphere. This is because of the high combustion temperatures associated with hydrogen, which are a result of its higher lower heating value (LHV). NO_x emissions at lower atmospheric levels can adversely affect human health, while at higher levels they can alter radiative forcing [21]. Consequently, NO_x is classified as an air pollutant, and regulations worldwide aim to mitigate its emissions to environmentally safe levels. Thus, ongoing research, such as the study of hydrogen flames in controlled environments, is critical to understanding how hydrogen can be utilised effectively while minimising its environmental footprint. The role of hydrogen in the energy transition must therefore be seen not only as a solution to carbon emissions but also as a challenge to be addressed in terms of NO_x emission control and flame stability.

1.2. Variation in Physical & Chemical Properties of Hydrogen

The physical and chemical properties of hydrogen differ significantly from those of kerosene, the conventional jet fuel. This distinction warrants further investigation to assess hydrogen's suitability as a future fuel for civil aviation. Below is a comparison of gaseous hydrogen and atomized kerosene [22,

23].

Hydrogen carries more energy per kilogram than kerosene, resulting in a higher LHV. However, its overall energy density is lower due to its much lower density. These characteristics lead to hydrogen having more than double the stoichiometric air-to-fuel (AFR) ratio and a higher maximum adiabatic flame temperature compared to kerosene. Furthermore, the autoignition temperature of hydrogen exceeds that of kerosene by more than 300 Kelvin (K), potentially due to the stronger bond between two hydrogen atoms compared to the bond between a carbon and a hydrogen atom.

Despite the higher autoignition temperature, the amount of energy needed to ignite a hydrogen-air mixture is significantly less, by about an order of magnitude, compared to the energy required for igniting a kerosene-air mixture [24]. This also results in a noticeably shorter ignition delay time compared to hydrocarbons, which is defined as the time interval between the first contact between the fuel and oxidizer and the onset of combustion. Due to its very low energy density, high diffusivity and reactivity, hydrogen burns with a laminar burning velocity approximately an order of magnitude greater than that of kerosene [25, 26]. Moreover, hydrogen has much broader flammability limits in air compared to kerosene or any other hydrocarbon fuel, ranging from 4% to 75%. This broad range is primarily due to the simplicity of hydrogen's combustion reaction mechanisms and pathways.

Hydrogen has a lower Lewis number (Le) than kerosene, which is defined as the ratio of thermal diffusivity (α) to mass diffusivity (D). In hydrogen, mass diffuses much quicker than heat due to the lower mass of the gas, resulting in a Lewis number less than one. Conversely, in kerosene, heat diffuses quicker than mass, leading to a Lewis number greater than one.

Additionally, due to the absence of strong intermolecular forces and the lightness of its molecules, hydrogen has an extremely low boiling point compared to kerosene and other hydrocarbon fuels. Hydrogen's lower flashpoint results from its broad flammability limits, low minimum ignition energy, and low boiling point. Because it evaporates at very low temperatures and can ignite at a very low flammability limit with little energy, its flashpoint is much lower than that of kerosene. The flashpoint is defined as the temperature at which a substance evaporates sufficiently to ignite in the presence of an ignition source. Consequently, hydrogen's freezing point is also significantly lower than that of kerosene.

1.3. Challenges Posed by the Combustion of Hydrogen

The development of gas turbines powered by hydrogen presents unique challenges, particularly with regard to issues such as a high propensity for flashback and high NO_x emissions. This section describes these challenges and the root causes of why they occur specifically in hydrogen combustion systems.

1.3.1. Higher Propensity for Flashback

Hydrogen combustion in gas turbines presents distinct challenges, particularly due to its higher susceptibility to flashback compared to conventional fuels like natural gas. Flashback refers to the undesirable upstream propagation of a flame into the fuel-air mixing region, potentially causing significant operational issues such as combustor damage and decreased efficiency. This phenomenon is particularly an issue with lean premixed combustion of hydrogen. Several factors contribute to this heightened risk of flashback in hydrogen combustion:

1. **High Flame Speed:** Hydrogen exhibits significantly higher laminar as well as turbulent flame speeds than hydrocarbon fuels. Lin et al. [27] demonstrated that hydrogen-rich fuel gases can have flame speeds several times greater than those of natural gas, which can surpass the flow speed, increasing the likelihood of the flame propagating upstream into the premixing zone. This

type of flashback is also known as a core flow flashback.

2. High Diffusivity: Hydrogen's high diffusivity and flame speed result in a more reactive environment, which can exacerbate the effects of turbulence. Ebi et al. [28] highlighted that turbulent flows can create complex interactions between the flame and the surrounding flow field, leading to conditions conducive to flashback.
3. Low Ignition Energy and Ignition Delay Time: As previously mentioned, hydrogen requires significantly less energy to ignite and has a shorter ignition delay time compared to kerosene, making it easier for the flame to ignite in the premixing duct/zone.

1.3.2. Higher NO_x Emissions

The combustion of jet fuel (kerosene) traditionally generates a range of pollutants beyond NO_x, including unburned hydrocarbons (UHCs), carbon monoxide (CO), and soot. The formation of these pollutants is strongly influenced by combustion temperature and the fuel-to-air equivalence ratio. Additional factors such as residence time, pressure, and combustor configuration also play a role in pollutant formation. Excluding these additional factors, figure 1.1 illustrates the trends in pollutant concentrations in relation to temperature and equivalence ratio [29, 30]. Since hydrogen as a fuel largely avoids the generation of contaminants such as UHCs, CO, and soot, NO_x becomes the primary concern. This issue is further amplified by the high combustion temperatures associated with hydrogen. As shown in figure 1.1, NO_x formation is strongly correlated with the peak combustion temperature.

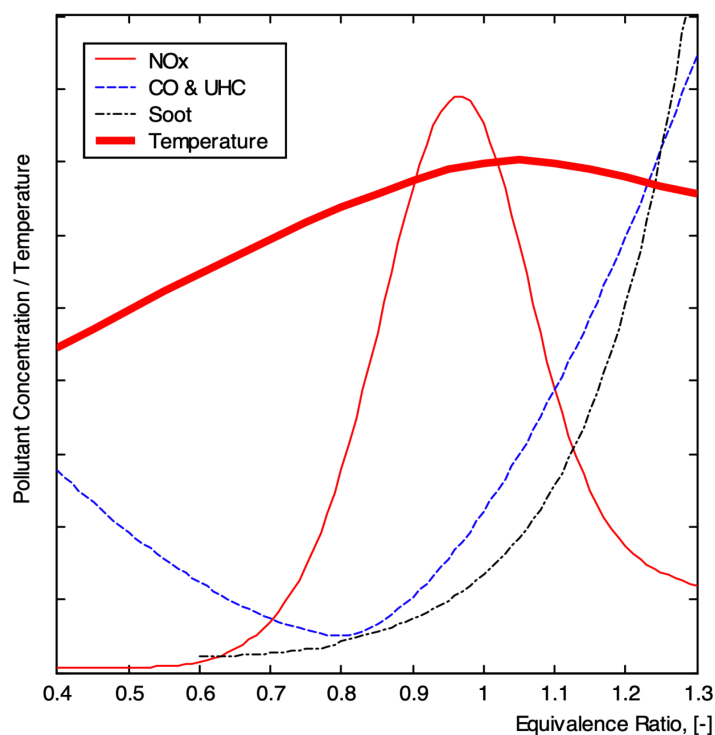


Figure 1.1: The variation in production of pollutants as a function of temperature and equivalence ratio (ϕ) [30]

The primary pathways for NO_x formation through the combustion of hydrogen include thermal NO, NNH-NO, and N₂O-NO pathways. These pathways are highlighted in figure 1.2.

The thermal NO pathway is the most well understood mechanism for the formation of NO_x in high-temperature combustion environments. It is characterised by the Zeldovich mechanism, provided in

equation 1.1[31, 32], where nitrogen and oxygen react at elevated temperatures to form NO. Reaction rates are highly sensitive to temperature, with significant increases in NO production observed as the combustion temperatures rise [33, 34].

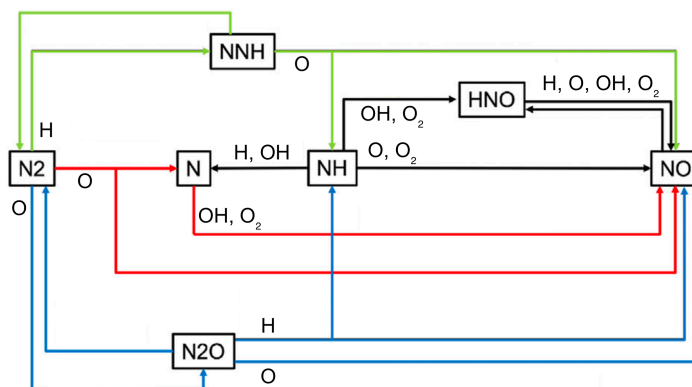


Figure 1.2: Simplified pathways for NO_x formation in hydrogen combustion [35]
(red for thermal NO, green for NNH-NO, black for NNH-HNO-NO, and blue for N₂O-NO)

The NNH pathway involves the formation of nitrogen hydride (NNH), which can subsequently react to produce NO. Hydrogen significantly enhances NO production through this pathway, as it facilitates the formation of NNH at lower temperatures. However, this pathway is not as prominent in NO_x formation as the thermal NO pathway which produces much more NO_x at higher temperatures [36, 37].

The N₂O pathway involves the formation of N₂O as an intermediate, which can then be converted to NO. This pathway is particularly relevant in combustion scenarios where oxygen levels are controlled, such as in staged combustion systems. Hydrogen can alter the reaction dynamics, potentially reducing the formation of N₂O and thus affecting the overall NO_x emissions profile [38, 36].

1.4. Strategies for Emission Control

A highly effective approach for reducing NO_x emissions involves the application of high Exhaust Gas Recirculation (EGR) rates, which redirects a fraction of the exhaust gases into the combustion chamber. This dilution of the air-fuel mixture results in a decrease in oxygen concentration and subsequently a reduction in the combustion temperatures. Ditaranto et al. [39] demonstrated that EGR can effectively limit combustion temperatures, thereby minimising NO_x formation in hydrogen-rich environments. This method is particularly relevant for hydrogen-fuelled gas turbines, addressing the unique challenges posed by its exceptionally high combustion temperatures.

Direct water injection is another promising strategy for reducing NO_x emissions. By cooling the combustion process, it effectively lowers combustion temperatures. Kotob et al. [40] reported that direct water injection, commonly referred to as a "wet cycle", can significantly reduce NO_x emissions in gas turbines. This method is particularly used for NO_x control in diffusion hydrogen combustion systems,

but the reduced combustion temperatures can negatively affect gas turbine cycle efficiency, potentially lowering both power output and overall energy conversion efficiency [41].

Additionally, lean premixed combustion technology plays a key role in NO_x reduction. By maintaining a lean fuel-to-air ratio, this approach reduces flame temperatures, which helps reduce emissions. Funke et al. [42] emphasised that lean premixed combustion is essential to achieve low NO_x emissions in hydrogen-rich fuel applications. Further, the use of micromix combustion technology, which improves fuel-air mixing, optimises combustion conditions and enhances NO_x reduction [43].

Catalytic combustion systems offer another innovative solution for controlling NO_x emissions. Alavandi et al. [44] reported the development of a catalytic combustor designed specifically for hydrogen turbines, achieving very low NO_x emissions while maintaining high efficiency. By leveraging catalytic reactions to promote more complete combustion at lower temperatures, these systems effectively reduce NO_x formation.

The integration of ammonia with hydrogen has been explored as an additional means of lowering NO_x emissions. Research indicates that ammonia can be used in conjunction with hydrogen to achieve reduced emissions, though additional systems, such as selective catalytic reduction (SCR), may be required to meet stringent NO_x limits [45].

1.5. Combustor Designs for Hydrogen Gas Turbines

To address the concerns brought up in previous sections of the report, a variety of specialised combustor designs have been engineered, each tailored to mitigate the specific combustion characteristics of hydrogen. These designs focus on controlling flame stability, managing fuel-air mixing, and reducing emission levels, while ensuring efficient and safe operation under hydrogen-rich conditions. This section explores the advancements in combustor technology aimed at overcoming the limitations posed by hydrogen combustion in gas turbines.

1.5.1. Diffusion Flame Combustor Designs

Figure 1.3 displays the GE10 Diffusive Flame Combustor from Cocchi et al. [46], which introduces steam into the combustion air via the external combustor head. This revealed a 30% reduction in NO_x emissions compared to the baseline, representing an effective compromise for 100% hydrogen diffusive flame applications in terms of emission control.

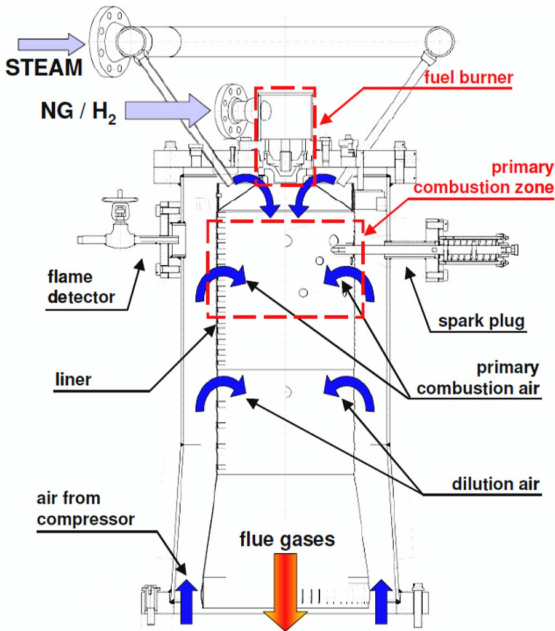


Figure 1.3: GE10 Diffusive Flame Combustor from Cocchi et al. [46]

Figure 1.4 displays the Turbtec T100 Combustor from Pappa et al. [47], which found that steam dilution in hydrogen enriched methane combustion prevented flashback by effectively lowering the reactivity of hydrogen, compared to the non-diluted case.

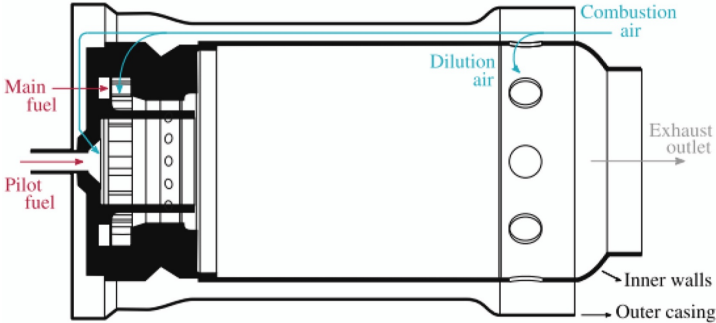


Figure 1.4: Turbtec T100 Combustor [47]

1.5.2. Premixed Combustor Designs

Figure 1.5 shows a modified TG50 DLN prototype combustor from Cappelletti et al. [48]. The prototype features a new swirler to enhance internal recirculation and a movable coflow fuel injection system for better control of mixing and flame flashback. The study evaluated two configurations for NO_x emissions and flashback limits, with the best performance (5-17 ppm for equivalence ratios of 0.25 to 0.34) achieved using nominal premixing without the pilot.

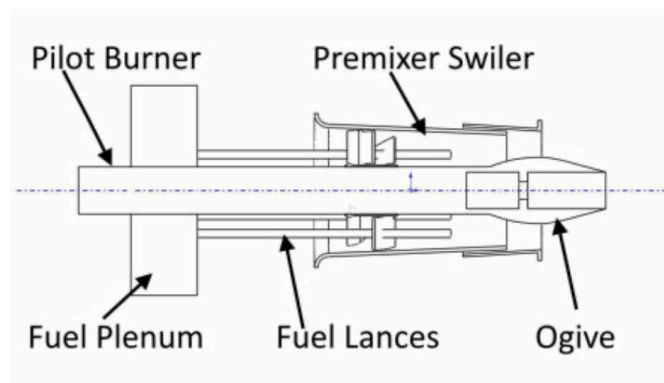


Figure 1.5: TG50 DLN Combustor Prototype [48]

Figure 1.6 shows a the design modifications for a new combustor compared to its conventional counterpart from Inoue et al. [49] that was developed that suppresses low flow velocity in the central swirling region to prevent flashback during hydrogen co-firing. This design has demonstrated the potential for gas turbine operation with up to 30% hydrogen by volume co-firing conditions.

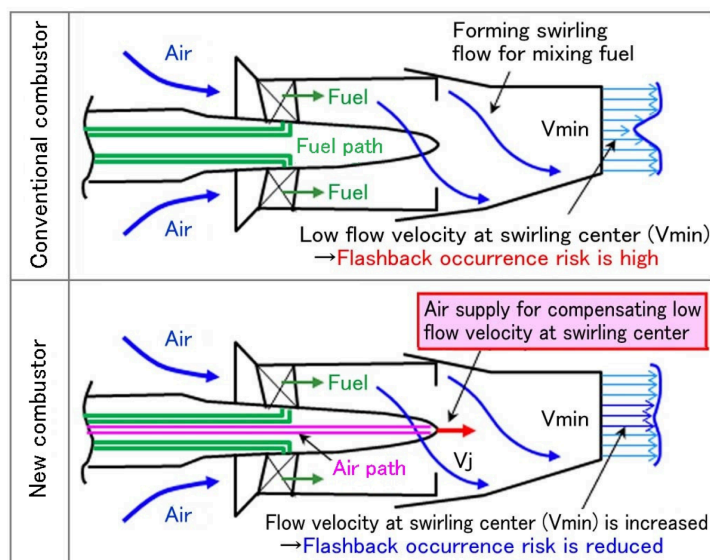


Figure 1.6: Conventional Combustor vs New Combustor Prototype from Inoue et al. [49]

1.6. Understanding Turbulent Combustion through Laminar Flames

The complexity of turbulent combustion, particularly in hydrogen-fueled systems, presents significant challenges for accurate modeling and control. One widely used approach to simplify the understanding of turbulent flame behavior is the study of laminar flames, which offers fundamental insights into the underlying combustion dynamics. By examining laminar flames, key characteristics such as flame structure, stability, and response to perturbations can be analyzed in a more controlled environment. These insights can then be extended to turbulent conditions, where interactions between strain rate, flow instabilities, and chemical reactions become significantly more complex.

An example of a setup that allows for the analysis of laminar premixed flames is the counterflow burner configuration, which is commonly employed in both experimental and numerical combustion studies. This geometry is particularly advantageous as it facilitates the formation of a stable, laminar flat flame,

allowing for easier measurement access and significantly simplifying mathematical modeling [50].

A study by Porcarelli et al. [35] demonstrated through numerical simulations that increasing the strain rate of lean, premixed and laminar hydrogen flames resulted in lower overall NO_x production. These simulations were conducted in a counterflow reactants-to-products configuration and at a lean equivalence ratio of 0.7.

Premixed hydrogen air flames are shown to be highly susceptible to various intrinsic instabilities, including both hydrodynamic (DL) and TD instabilities. The impacts of these instabilities can be quantified by performing a flame stability analysis and observing the dispersion relations in the linear regime. One such analysis by Berger et al. [51] found that imposing slight sinusoidal perturbations to the flame-front of unstretched premixed hydrogen flames led to exponential growth of the perturbations in the linear regime. The destabilising effects of the instabilities were especially prominent at leaner equivalence ratios, because of the differential diffusion effects of hydrogen as a fuel. However, due to the unstretched and unstrained nature of the flame configuration in the simulations, the wavelength (wave number) of the perturbation imposed remained largely unchanged for the duration of the linear regime.

In a strained counterflow reactants-to-products configuration, however, there are velocity gradients both across and tangential to the flame-front. These tangential velocity gradients are likely to influence the shape of the flame-front in the event of a perturbation. To explore whether this effect is stabilising or destabilising to the flame, Direct Numerical Simulations (DNS) of the flame can be performed for a perturbed flame-front in a similar counterflow reactants-to-products setup.

2

Research Background

This section of the report delves into various phenomena that significantly influence the behaviour of hydrogen flames, such as Markstein number effects, intrinsic flame instabilities, etc., providing a comprehensive background for subsequent analysis.

2.1. Markstein Number Effects

2.1.1. Summary

The flame speed has further potential to vary due to the Markstein number (stretch) effects and cellular instabilities. Stretch (K) is defined in equation 2.1 [52].

$$K = s_L^0 \kappa + S \quad (2.1)$$

Where s_L^0 denotes the unstretched laminar flame speed of hydrogen, κ denotes the curvature, and S is the strain rate of the flame. The stretch equation multiplied by a negative value of the Markstein length ($-\mathcal{L}$) determines how the burning velocity varies due to stretch effects as shown in equation 2.2 [52]. Markstein length (\mathcal{L}) is a parameter used in the study of combustion, especially in relation to flame propagation within gaseous mixtures, and it quantifies the impact of flame stretch on the speed of a premixed flame. Furthermore, it indicates how preferential diffusion influences the stability of a flame [53].

$$s_L = s_L^0 - s_L^0 \mathcal{L} \kappa - \mathcal{L} S \quad (2.2)$$

Asymptotic analysis and experimental observations indicate that flame speed varies linearly with flame stretch, with the Markstein length governing this relationship [54]. The Markstein length of mixtures is said to be dependent on physical and chemical properties such as the global activation energy associated with the reaction, the thermal expansion coefficient and the effective Lewis number of the mixture. This is calculated with the Lewis numbers of the fuel and/or the oxidiser and it depends on the equivalence ratio (ϕ) [55]. This becomes a very important parameter for hydrogen-air flames, as hydrogen has a Lewis number that is considerably lower than 1, which can result in a negative Markstein lengths for very lean hydrogen-air mixtures. This would have the effect of further increasing the burning velocity where the flame is stretched (positively curved or strained) locally.

$$\mathcal{M} = \frac{\mathcal{L}}{\delta_L} \quad (2.3)$$

The Markstein number (\mathcal{M}) is defined by equation 2.3 [52], in which \mathcal{L} is the Markstein length, and δ_L is the characteristic laminar flame thickness. As the Markstein number is said to rely on various physical and chemical properties of the flame, Bechtold et al. [55] attempts to model the relationship between the Markstein number and the equivalence ratio of a specific fuel-air mixture exclusively. The predictions of this theory are displayed below in figure 2.1, in which hydrogen-air mixtures at a very lean equivalence ratios do exhibit a negative Markstein number. As the equivalence ratio is increased towards stoichiometric conditions, however, the sign of the Markstein number changes to positive (at approximately $\phi = 0.8$).

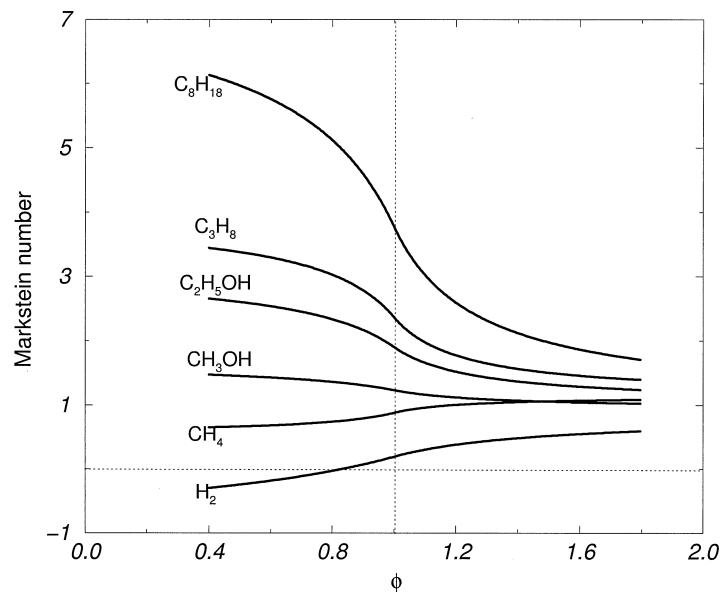


Figure 2.1: The Markstein number (\mathcal{M}) for various fuel-air flames, varying with equivalence ratio (ϕ) [55]

2.2. Intrinsic Flame Instabilities

Intrinsic flame instabilities are a local phenomena and are defined as instabilities that do not occur as a result of pressure waves or oscillations [52]. The combustion of lean hydrogen flames is increasingly susceptible to these types of instabilities such that flame shapes, heat release rates, and flame dynamics may be affected. The interplay between these instabilities and turbulence is not particularly well understood, and the instabilities themselves are challenging to predict and control. The types of these instabilities that are important to consider for lean hydrogen flames are as follows [52]:

- **Hydrodynamic / Darrieus–Landau (DL) Instability** [56]: Hydrodynamic, or Darrieus–Landau (DL) instability is an instability that occurs in premixed flames and occurs as a result of the sudden variation in density across the flame. It is always destabilising to the flame as the change of the streamlines results in the flow in front of the flame slowing. This phenomenon is demonstrated in figure 2.2.

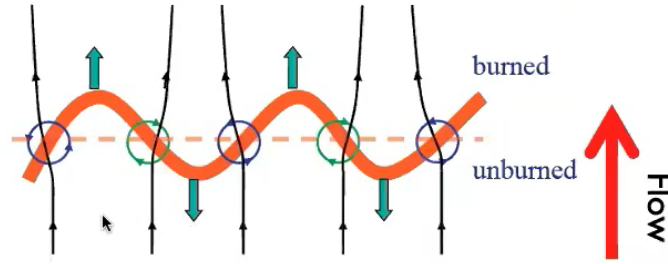


Figure 2.2: Diagram depicting Darrieus-Landau (hydrodynamic) instability [57]

DL instability's growth rate depends solely on the expansion ratio of the flame σ , which is defined in equation 2.4, where ρ_u is the unburned and ρ_b is the burned density of the flame [58].

$$\sigma = \frac{\rho_u}{\rho_b} \quad (2.4)$$

The growth rate is then given by equation 2.5 [58]. The variables for growth rate $\bar{\omega}$ and wave number \bar{k} in equation 2.5 are dimensionless quantities.

$$\bar{\omega} = \omega_{DL} \bar{k} \quad \text{where} \quad \omega_{DL} = \frac{\sqrt{\sigma^3 + \sigma^2 - \sigma} - \sigma}{\sigma + 1} \quad (2.5)$$

These quantities are normalised with the flame time τ_F and the flame thickness l_F , respectively, as detailed in equation 2.6 [58].

$$\bar{\omega} = \omega \tau_F \quad \text{and} \quad \bar{k} = k l_F \quad (2.6)$$

- **Thermodiffusive (TD) Instability** [56]: Thermodiffusive instability arises from a significant disparity between the thermal diffusivity of a mixture and the molecular diffusivity of the fuel. As the Lewis number for hydrogen is very low, the hydrogen itself diffuses much quicker than the air in the mixture (known as differential diffusion), which can lead to locally rich or lean equivalence ratio. This also results in the development of specific cellular structures in the flame. There exist theoretical derivations of the growth rate due to this phenomenon, notably by Matalon et al. [58] for mixtures with an effective Lewis number close to one, as well as by Sivashinsky [59] for mixtures which assume no or a negligible variation in density across the flame (no hydrodynamic instability).

The effects that these instabilities have on the consumption speeds of the flame vary. For example, the DL instability on its own was observed to moderately enhance burn rates through an increase in flame surface area [56, 60, 61]. In contrast, TD instabilities were found to significantly accelerate the consumption speeds of laminar flames [51], and their presence was markedly amplified by concurrent DL instabilities. The transport occurring in turbulent flames is generally considerably greater than molecular diffusion, which is why the effects of the TD instability would be expected to be masked almost completely (as the TD instability arises from molecular effects). However, Berger et al. [62] demonstrated that, in lean hydrogen flames, turbulence actually intensifies these instabilities.

2.2.1. Study

Berger et al. [62] employed large-scale DNS to explore the interplay between TD instabilities and turbulence in lean premixed turbulent hydrogen/air flames. Two similar DNS cases were conducted, one with realistic transport models which are able to accurately predict TD instabilities and another with a Lewis number of 1 for all species. The thermodynamically unstable flame exhibited enhanced turbulent flame speed as a result of substantial changes in the local reaction rates, driven by locally fluctuating equivalence ratios which were caused by differential diffusion. Comparisons with a thermodynamically unstable laminar flame revealed that the turbulent flame experienced greater variations in equivalence ratio and reaction rates, largely due to increased curvature fluctuations and a higher mean strain rate caused by turbulence. The interaction between turbulence and TD instabilities resulted in a noticeably higher rate of fuel consumption per unit of flame surface area. Furthermore, the study found that the creation of surface area of the flame due to the strain rate was similar in both, the thermodynamically unstable and stable flames and primarily influenced by small-scale turbulence. For curvature effects, it was noted that the reduction of surface area in cusp regions was comparable between the flames, but that the unstable flame demonstrated a considerable increase in flame surface area in convex regions facing the reactants, resulting in the emergence of finger-shaped formations that were absent in the stable flame. These structures, along with surface area changes due to curvature, were more pronounced in the turbulent unstable flame, suggesting a significant interplay between turbulence and instabilities.

2.2.2. Implications for Thesis Methodology

Based on the findings of Berger et al. [62], it is essential to employ accurate transport models that account for the low Lewis number of hydrogen to properly capture the effects of TD instabilities. Although this thesis focuses on premixed laminar hydrogen flames, these instabilities, along with hydrodynamic instabilities, can significantly influence flame behavior, particularly in perturbation growth. Therefore, realistic transport models are critical to accurately simulate the complex interactions and ensure reliable predictions of flame dynamics in the DNS simulations.

As also discussed in the previous section, hydrogen exhibits a negative Markstein number at lean equivalence ratios (below 0.8), indicating that the laminar burning velocity increases in response to curvature and strain. These lean conditions are also associated with destabilising TD instabilities, while the DL instability, driven by the sudden variation in density over the flame front, consistently acts as in a destabilising manner. Given these factors, an equivalence ratio of 0.7 presents an intriguing case for investigation, as the combined effects of these instabilities are likely to significantly influence the evolution and structure of the flame front.

2.3. Thermoacoustic Instabilities

Thermoacoustic instabilities arise due to "the dynamic interaction between unsteady heat release and acoustic perturbations" within a combustion system [63]. These instabilities often manifest as self-sustaining, large-amplitude oscillations. Unsteady heat release serves as an effective energy source, producing pressure waves within the combustor. These waves travel through the chamber, some are reflected partially off various components, such as the walls or the plenum. Upon re-entering the zone of combustion, the reflected acoustic waves alter the flame, modulating the flow conditions and inducing further unsteady heat release, thus closing the feedback loop. If the acoustic pressure is in phase with the unsteady heat release, it leads to the intensification of the acoustic pressure fluctuations, potentially leading to self-excitation of the acoustic waves. This phenomenon is described by Rayleigh's criterion, where the correlation between pressure fluctuations and the heat release drives the system towards insta-

bility [64]. Self-sustained oscillations of thermoacoustic instabilities are an undesirable phenomenon in combustion chambers of gas turbines and aeroengines [63]. Although thermoacoustic instabilities are traditionally linked to the geometry and acoustic modes of the system, recent research has revealed the existence of intrinsic thermoacoustic instabilities. These intrinsic thermoacoustic instabilities occur independently of the combustor geometry and are sustained purely through the interaction between fluctuating heat release and the flow field, particularly in premixed combustion. Even with highly anechoic boundary conditions, intrinsic thermoacoustic instabilities can arise due to the sensitivity of premixed flames to velocity perturbations, which alter the heat release and close the feedback loop, making them a key area of interest in combustion studies [63, 64].

2.3.1. Study

A study by Yao [64] investigating hydrogen flames in a counterflow opposed jet setup revealed that thermoacoustic instabilities are significantly amplified when perfectly reflecting boundary conditions are applied, particularly in high strain rate cases. The analysis showed substantial acoustic perturbation growth, with standing wave behaviour and dominant modes identified through spectral methods. When forced sinusoidal pulses were introduced, the high strain rate case exhibited amplification over a broader frequency range compared to the low strain rate case.

2.3.2. Implications for Thesis Methodology

The findings regarding thermoacoustic instabilities in diffusion flames suggest that similar instabilities may also be present in a counterflow reactants-to-products setup. Given this potential for instabilities, it is crucial to consider the implementation of Navier-Stokes Characteristic Boundary Conditions (NSCBC) at the inlets and outlets of the computational domain. These boundary conditions are designed to allow a controlled amplitude of pressure waves to pass through and exit the domain while partially reflecting them back into the flow. This reflective behaviour can help manage the instabilities that might arise during the simulations, provided that it is modelled after the physical reflective properties of combustion chamber walls.

The methodology for implementing NSCBC and selecting the appropriate parameters will be detailed further in the methodology section of this thesis. Properly configuring these boundary conditions is critical in accurately capturing the acoustic waves and promoting a more reliable representation of the physical processes within the counterflow setup.

2.4. Differential Diffusion Effects

2.4.1. Derivations and Summary

Differential diffusion effects occur under the same conditions as the TD instability, i.e., when there is a considerable difference between the thermal diffusivity of a mixture and molecular diffusivity of a fuel. However, differential diffusion effects are a one dimensional phenomenon which describe the variation in diffusion of a species across the flame front, whereas the TD instability is a two dimensional phenomenon which combines the differential diffusion effects with the curvature and the strain rate of the flame at different positions. Computational fluid dynamics (CFD) simulations require that the equations describing the conservation of mass, momentum, and energy be solved. In reacting flows involving multiple different species, however, additional equations for the conservation of each species need to be solved (shown in equation 2.7) [65].

$$\frac{\partial \rho Y_m}{\partial t} = \frac{\partial (\rho(u_i + V_{m,i})Y_m)}{\partial x_i} = \dot{\omega}_m \quad \text{where} \quad m = 1, 2, \dots, M \quad (2.7)$$

In which t is the time, ρ is the density of the mixture, M is the total number of species, and subscript m refers to a specific species in the mixture, Y_m is the mass fraction, x_i , u_i , and $V_{m,i}$ are the spacial coordinates, velocity components, and diffusion velocity components for dimensions $i = 1$ to 3 respectively, and finally, $\dot{\omega}_m$ is the reaction rate. Equations 2.8 can be derived by combining equation 2.7 with the conservation of mass equation [65].

$$\sum_{m=1}^M Y_m V_{m,i} = 0 \quad \text{and} \quad \sum_{m=1}^M \dot{\omega}_m = 0 \quad (2.8)$$

The diffusive velocities of the all the species are obtained by solving the multi-component diffusion equation (equation 2.9) [65].

$$\begin{aligned} \nabla X_j = & \sum_{m=1}^M \frac{X_j X_m}{D_{jm}} (V_m - V_j) + (Y_j - X_j) \frac{\nabla P}{P} + \frac{\rho}{P} \sum_{m=1}^M Y_j Y_m (f_j - f_m) \\ & + \sum_{m=1}^M \frac{X_j X_m}{\rho D_{jm}} \left(\frac{\alpha_m}{Y_m} - \frac{\alpha_j}{Y_j} \right) \frac{\nabla T}{T} \quad \text{for } j = 1, 2, \dots, M \end{aligned} \quad (2.9)$$

Where subscripts j and m refer to the species in a mixture, X is the molar fraction, D_{jm} denotes the binary mass diffusion coefficient of species j into m , f is a volume force, α is the thermal diffusivity, and T and P are the temperature and pressure of the mixture. The consecutive terms located on the right side of the equation represent the Stefan-Maxwell, pressure induced diffusion, body force induced diffusion, and thermal diffusion (Soret effect) terms respectively. The binary mass diffusion coefficient varies with molecular parameters of the species involved as well as the thermodynamic parameters such as pressure and temperature. For unsteady flows, this equation requires solving in each direction for each instant in time and point in space, which makes it very difficult and costly to solve. Additionally, the system is linear of a size N^2 .

For simpler cases involving only two species in a mixture with low pressure and temperature gradients, and negligible body forces, equation 2.9 can be simplified into equation 2.10 [65].

$$\nabla X_1 = \frac{X_1 X_2}{D_{12}} (V_2 - V_1) \quad (2.10)$$

As the mass fraction of the two species add up to 1 and with the help of equation 2.8, equation 2.10 can be re-written as equation 2.11, also known as Fick's law [65].

$$V_1 Y_1 = -D_{12} \nabla Y_1 \quad (2.11)$$

For a mixture with more than two species, a mixture-averaged approach for the mass diffusion coefficient can be used (also known as the Wilke model or the Hirschfelder and Curtiss approximation), as shown in equation 2.12.

$$V_m X_k = -D_m \nabla X_m \quad \text{where} \quad D_m = \frac{1 - Y_m}{\sum_{j \neq m} X_j / D_{jm}} \quad (2.12)$$

This allows for the calculation of a mass diffusion coefficient of a single species into the entire mixture, which subsequently can be substituted back into equation 2.7 for the following modified species conservation equation (equation 2.13), where W is the average molecular weight of the entire mixture, W_m denotes the molecular weight of the species m , and coefficient D_m denotes the effective coefficient of diffusion of species m into the whole mixture.

$$\frac{\partial \rho Y_k}{\partial t} + \frac{\partial \rho u_i Y_k}{\partial x_i} = \frac{\partial}{\partial x_i} \left(\rho D_k \frac{W_k}{W} \frac{\partial X_k}{\partial x_i} \right) + \dot{\omega}_k \quad \text{where} \quad \frac{1}{W} = \sum_{k=1}^N \frac{Y_k}{W_k} \quad (2.13)$$

Equation 2.13 also allows for the calculation of the mass diffusion constants using other models, such as unity and constant Lewis number models. In these models, the Lewis number for every species is either set to one or a pre-determined value for the particular species, which is then used to obtain the diffusivity of a species in the mixture as shown in equation 2.14.

$$D_k = \frac{\alpha}{1} \quad \text{or} \quad \frac{\alpha}{Le_k} \quad (2.14)$$

As all species share a single value for their diffusion coefficient in the unity Lewis number model, it is said to not be very accurate for hydrogen flames, whereas the constant Lewis number model is generally more accurate as it takes the extremely low Lewis number of hydrogen into account.

Finally, there have been attempts to solve the full multi-component diffusion equation using various methods. One such method involved direct numerical inversion of the transport linear systems derived from kinetic theory, but was found to be incredibly computationally demanding. Another method used empirically averaged expressions, but was found to deliver inaccurate transport coefficients. Therefore, Ern and Giovangigli [66] proposed a third, iterative method to obtain approximate solutions of the transport linear systems which then used truncation to provide approximate expressions of reasonable accuracy for all the transport coefficients. This method was then coded into a Fortran library named EGLIB [67].

2.4.2. Studies

In a study by Ern and Giovangigli [68], it was demonstrated that in counterflow laminar premixed steady hydrogen-air flames, extinction limits, characterised by the equivalence ratio or strain rate, exhibited sensitivity to multi-component transport. This sensitivity was particularly pronounced in richer hydrogen flames. Notably, omission of thermal diffusion in these flames resulted in a significant over-prediction of the strain rate at extinction, reaching up to 36%.

Abbasi-Abiteh and Bergthorson [69] investigated the role of differential diffusion on flame velocities in both laminar and turbulent counterflow setups under high strain conditions. Their study focused on

premixed methane and propane flames that were enriched with hydrogen, each representing different effective Lewis numbers (Le_{eff}), while keeping the same laminar flame speed. Instantaneous flame position probability density functions (PDFs) showed that differential diffusion became noticeable in hydrogen-enriched flames when Le_{eff} was less than 1, with its effects becoming particularly significant below 0.8. In turbulent counterflow flames under high strain, the shape of the flame front was influenced by differential diffusion in mixtures with $Le_{\text{eff}} < 1$. Although the overall strain rates remained steady, an increase in flame curvature was observed when Le_{eff} dropped below a value of one.

Grear et al. [70] compared the differences in the results of freely propagating, lean, premixed, hydrogen flames simulated with the full multi-component transport model with cross-diffusion (with Soret and Dufour effects) as well as with the mixture-averaged transport model. The study found that the multi-component model predicted higher local and global flame propagation speeds, as well as a higher fuel enrichment in the flames due to the positive curvature and TD effects compared to the mixture-averaged model. Additionally, it found that the cellular formations of the thermodynamically unstable flame were reduced in size and exhibited a higher propensity to either fragment or be suppressed when analysed using the multi-component model. Ultimately, the research indicated that the temperature gradient associated with the Soret effect and peak temperatures of the flames observed were greater in the multi-component model than in the mixture-averaged model.

Fillo et al. [71] is another study which assessed the impact of multi-component diffusion in premixed, 3D distributed/broken hydrogen flames, as well as a 2D, unstable hydrogen flame, with the aim of investigating the accuracy of mixture-averaged diffusion models compared to multi-component diffusion models. The study found that mixture-averaged diffusion produced differences of 10–20% in diffusion flux vectors on average, with discrepancies exceeding 40% in zones with pronounced flame curvature. Despite these localised differences, global flame statistics showed smaller variations between the models. Variations in normalised turbulent flame speeds ranged from 5–20%, corresponding to variations of 5–10% in highest fuel source rates. The study also noted that the distinctions between the two diffusion models became more pronounced with increasing flame curvature and species gradient magnitude, particularly in three-dimensional turbulent flames, where steep and highly variable scalar gradient fields led to multi-directional diffusion effects. In contrast, for an unsteady, 2D laminar hydrogen flame, where vectors of the species gradient were largely aligned with the flow direction, the mixture-averaged model matched the accuracy of the multi-component model to 98%, even near regions of thermal instability. This suggests that while the mixture-averaged diffusion model performs well in simpler, laminar configurations, its accuracy diminishes in more complex three-dimensional turbulent flames due to the increased variability in scalar gradients and multi-directional diffusion.

2.4.3. Implications for Thesis Methodology

The studies on differential diffusion stress the importance of accurately modelling transport processes, especially in hydrogen flames where multi-component transport plays a significant role. As highlighted by Ern and Giovangigli [68] and others, multi-component transport, including thermal diffusion, is crucial for predicting flame behaviour under high strain conditions.

In the software used, three diffusion models were available: the single species diffusion model, the mixture-averaged diffusion model, and the Schmidt species diffusion model, which allowed each species to have its own Schmidt number. The Schmidt species diffusion model was not selected as in reality, the Schmidt number of species varies with the temperature, and because there are significant temperature variations present in the domain, ranging from unburned gases to adiabatic and super-adiabatic conditions. The mixture-averaged diffusion model was chosen because as it directly accounts for local temperature variations when determining species diffusivities, ensuring a more accurate representation of differential diffusion effects across these varied thermal fields.

Fillo et al. [71] has shown that for two-dimensional, unsteady, laminar hydrogen flames, where species gradient vectors predominantly align with the flow direction, the mixture-averaged diffusion model achieves results closely matching those of the multi-component diffusion model, with less than 2% discrepancy, even in regions of thermal instability. Although the present work involves perturbing a 2D laminar flame to generate a sinusoidal flame front, the curvature variations are less pronounced than those in the unsteady flame studied. Therefore, the mixture-averaged model is expected to maintain high accuracy. Additionally, in the strained counterflow flame configuration, certain regions, particularly near the outlet, may exhibit misalignment between the flow direction and the species gradient vectors. This misalignment can increase mass diffusion, potentially amplifying intrinsic instabilities such as the TD instability. While these instabilities are not inherently desirable, their amplification may lead to the breakup of the flame front as it transitions from a steady to an unsteady state. Understanding whether this transition occurs is crucial for future research into the viability of hydrogen in combustion chamber applications.

2.5. Soret Effect

2.5.1. Summary

The Soret effect (also known as thermodiffusion and thermophoresis) is, in the simplest terms, defined as mass diffusion that occurs in the presence of temperature gradients. This is a particularly important effect for mixtures containing molecules with a large variation in mass and large temperature gradients, as this effect is known to diffuse lighter molecules towards the colder regions and heavier molecules towards the hotter regions in a temperature gradient [72, 73]. Due to the lightness of hydrogen molecules, this is likely to have a significant effect on its diffusion in flames, and therefore must be accounted for in numerical simulations for accurate results.

2.5.2. Studies

Yang et al. [74] conducted a computational study examining the individual and combined impacts of thermophoresis of hydrogen molecules (H_2) and radicals (H) on free propagating planar premixed hydrogen–air flames. Additionally, the investigation also explored the extinction due to strain of premixed and non-premixed counterflow flames. Results showed that, in non-freely propagating planar flames, the thermophoresis of H_2 increased the concentration of fuel within the flame structure. This alteration modified the mixture stoichiometry and flame temperature, resulting in a significant increase in flame speed for lean mixtures. Thermophoresis of the H radical influenced its concentration levels and dispersion in the reaction zone, subsequently impacting individual reaction rates. Specifically, in a counterflow, symmetric twin flame configuration with premixed flames, particularly very close to extinction, reaction rates may increase for lean flames. This was primarily due to the active reaction regions being situated at the stagnation surface.

2.5.3. Implications for Thesis Methodology

In this study, the growth rate of laminar premixed flames is modeled by considering the influence of intrinsic instabilities and tangential strain rates. One critical aspect identified in the literature is the role of thermophoresis of H_2 , which significantly affects flame dynamics by altering the effective Lewis number.

Given the understanding from Yang et al. [74], it is imperative to incorporate the effects of thermophoresis into the diffusion model. The increase in flame speed due to reduced effective Lewis numbers is

expected to influence the intrinsic instabilities and the associated growth rates. Therefore, accurately accounting for this phenomenon is essential for a comprehensive analysis. However, upon review of the capabilities of the simulation software used, it was noted that there is no explicit option related to the implementation of thermophoresis (Soret diffusion) of hydrogen in the software or its manual. This suggests that thermophoresis may be enabled by default or is not available as a configurable parameter within the simulation environment. Consequently, the absence of this modelling feature necessitates careful consideration when interpreting simulation results and their implications for flame dynamics.

2.6. More Numerical Simulations of Hydrogen Flames

Berger et al. [75] conducted "large-scale two-dimensional numerical simulations of thermodiffusively unstable lean premixed hydrogen flames using detailed finite rate chemistry". The simulations involved extended integration times and expansive domain sizes to eliminate confinement effects on flame front dynamics. Regardless of domain size, the flame consumption speed became independent. The smallest length scales in the unstable structure of the flame front (marked by local cusps) were found align closely with the least stable wavelength estimated through linear stability analysis. The largest flame intrinsic structures, termed flame fingers, emerged from the interplay of small-scale cusps. These flame fingers periodically formed and disintegrated due to TD instability, without the appearance of a global cusp as seen in purely hydro-dynamically unstable flames. The limited size of the largest fingers stemmed from instability in their motion, leading them to tilt and shift laterally, ultimately rejoining the flame. Investigations of the unburnt gas temperature and equivalence ratio indicated that flame fingers only developed in thermodiffusively unstable flames.

In a thermodiffusively unstable premixed hydrogen flame, Wen et al. [76] observed the presence of cellular flame structures driven by strong differential diffusion of hydrogen, resulting in varying curvature and strain rates. The complex cellular flame structures significantly impacted NO formation pathways due to the different species exhibiting sensitivity to the curvature of the flame front as well as differential diffusion effects. The study investigated NO formation characteristics in this context, analysing elementary reaction rates and reaction fluxes conditioned on curvature values. The research demonstrated that curvature has a direct influence on NO formation, notably affecting dominant NNH and NO reaction pathways, whereas the impact of the thermal-NO pathway was deemed negligible according to an initial analysis using a flamelet model. A study by Day et al. [77] also suggested that the preferential diffusion of hydrogen led to local hotspots that exhibited intensified burning compared to idealised steady flames, which in turn led to excess NO production, especially at lower equivalence ratios.

Finally, Porcarelli and Langella [78] found that the use of a multi-component diffusion model showed significant variation in mixture fraction values across a strained and premixed lean hydrogen flamelet compared to the unity Lewis number model. This variation was significant for both the unstretched and stretched cases. In the unstretched case, the mixture fraction was shown to rapidly decrease at lower values of the progress variable, and then gradually increase return to its original value as the progress variable increased to 1. As the strain rate was increased, the mixture fraction curve was found to shift upwards with very minor variations to the overall shape of the curve. This indicated an overall enrichment of the mixture within the flame-front due to increased strain. Acquaviva et al. [79] also verified these same results by plotting the local equivalence ratio across premixed hydrogen flamelets, which was shown to follow the same initially decreasing and then increasing trend. Additionally, the study also exhibited the effects of including Soret diffusion, which resulted in locally leaner mixtures at a low progress variable, and locally richer mixtures at a higher progress variable.

2.7. NO_x Trends in Strained Hydrogen Premixed Laminar Flames

The study by Porcarelli et al. [35] attempted to numerically simulate NO_x emissions of lean ($\phi = 0.7$), laminar, premixed, and highly strained hydrogen flames. Two high strain rates ($a = 2000\text{s}^{-1}$ and $a = 5000\text{s}^{-1}$) were investigated in 2D. The simulations consistently demonstrated a decreasing trend in NO_x emissions with increasing strain rate. The density-weighted NO integral exhibited the same trend, with 1D and 2D integrals maintaining a nearly direct proportionality, indicating that the suppression of NO_x was not offset by increase NO production in the tangential direction to the flame front. The study also used 2D streamline analyses at different strain rates to prove that no extra NO was formed in the direction tangential to the flame at elevated strain rates and that the reduction of NO_x at higher strain rates was not due to the shorter residence time. Comparison of different strain rates showed that the thermal pathway was responsible for greatest decrease in NO formation than all other NO formation pathways combined. This decrease was largely due to the reduction in dissociation of N₂ into N radicals. Peak mass fractions of key radicals, except O radicals, increased with higher strain rates, leading to elevated NO formation near the flame due to increased presence of H and N radicals. However, at the highest strain rates, downstream concentrations of free radicals decreased, limiting NO formation through the thermal pathway despite higher formation near the flame.

2.8. Intrinsic Instabilities in Premixed Hydrogen Flames

The study by Berger et al. [51] investigated the influence of intrinsic instabilities in lean hydrogen premixed flames through numerical simulations under varying conditions. It emphasised the role of both the DL (hydrodynamic) instability and TD instabilities, which induce substantial wrinkling of the flame front, leading to the complex formation and breakdown of cellular structures. Since theoretical models were unable to accurately predict the evolution of these instabilities, the study numerically analysed the behaviour of flames subjected to harmonic perturbations. During the initial linear phase, the variation of the perturbation amplitude was measured, providing insight into the influence of intrinsic instability mechanisms and their dependence on the perturbation wave number, resulting in characteristic dispersion relations. The study found that reducing the equivalence ratio enhanced instability growth rates. A detailed analysis of the dispersion relations revealed their dependence on parameters such as the expansion ratio, the effective Lewis number, and the Zeldovich number. Although theoretical models were unable to quantitatively capture the observed numerical dispersion relations across different conditions, the study noted that trends related to these parameters were qualitatively captured. The findings underscored the tendency of lean hydrogen flames to experience instabilities in environments pertinent to real-world combustion systems, like heaters and gas turbines.

The second part of the study by Berger et al. [80] observed the long-term behaviour of lean premixed hydrogen flames, which exhibited significant corrugation, flame speed increase, as well as fluctuations in local reaction rates. The study observed local extinction events, peaks in reaction rates, and variations in burnt gas temperatures, both sub-adiabatic and super-adiabatic. Additionally, alterations in local flame thickness were noted, indicating that the reactivity of the flame significantly deviated from that of a non-stretched laminar flamelet. The influence of the instabilities was found to increase with decreasing equivalence ratios and unburned temperatures, or with rising pressure, highlighting the relevance of these findings for combustion systems operating at high pressures in agreement with the stability analysis from the earlier study. The research provided a quantitative analysis of how key flame parameters impacted flame speed increases. Importantly, the flame speed enhancement resulting from instabilities showed a strong correlation with the maximum perturbation growth rates reported in the initial part of the study, illustrating a clear relationship between short-term instability development and long-term flame behavior.

2.9. Identifying a Gap in the Literature

The study by Porcarelli et al. [35] serves as a pivotal reference for the current methodology, particularly due to its counterflow configuration, which effectively reduces NO_x emissions in premixed laminar hydrogen flames by tangentially straining the flame. Although the study provides valuable information about emission control, it primarily emphasises NO_x emissions without delving into the analysis of flame stability under varying conditions. In contrast, the work of Berger et al. [51, 80] investigates the stability of flame fronts through sinusoidal perturbations, significantly contributing to our understanding of flame dynamics. However, Berger et al.'s approach does not consider the effects of strain on flame stability.

To bridge this gap, the current methodology synthesises the counterflow setup of Porcarelli et al. with the perturbation analysis from Berger et al. This combination allows for a comprehensive examination of flame stability within a strained configuration, which has the potential to lower NO_x emissions. The integration of these methodologies enables the investigation of how sinusoidal perturbations impact the growth rates of instabilities, influenced by factors such as wavelength, amplitude, and strain rate.

2.10. Research Questions

1. What is the effect of tangential strain on the stability of perturbed laminar lean premixed hydrogen flames?
 - (a) What is the mechanism through which tangential strain affects the stability of perturbed flame fronts?
 - (b) What are the effects of varying the amplitudes and wavelengths of the initial perturbations imposed on the flame fronts?
 - (c) Are there indications of thermoacoustic instabilities present in a strained counterflow setup, and how does the strain rate influence these instabilities?

Combustion Mechanisms for Hydrogen

3.1. GRI-Mech 3.0 [81]

3.1.1. Overview

The GRI-Mech 3.0 is a mechanism designed by the Berkeley combustion team to model natural gas combustion, NO_x formation, as well as reburn chemistry (to reduce NO_x to N_2). It has a comprehensive "compilation of 325 elementary chemical reactions, rate coefficients, and thermochemical parameters involving 53 species" and it supersedes earlier versions, offering updated and expanded kinetics and target data. Optimised for conditions ranging from equivalence ratios of 0.1 to 5 for premixed systems, 1000 to 2500K and 0.01 to 10 atm, the mechanism demonstrates superior overall performance within these ranges. While caution is advised when using it beyond these limits, the model's reliance on current elementary reaction rate theory enhances its applicability. Notably, GRI-Mech 3.0 does not account for the chemistry of "selective non-catalytic reduction of NO_x ", which may be significant at lower temperatures (1033K - 1363K) in specific cases involving mixing with ammonia or urea. Primarily designed for methane and natural gas, caution is urged when applying GRI-Mech 3.0 to model combustion of pure fuels not covered in its optimization targets.

3.1.2. Validation Data

Planke et al. [82] asserts that while the GRI-Mech 3.0 is optimised for the combustion of natural gas, and not specifically for hydrogen, it can be considered partially validated for the stoichiometric combustion of hydrogen and air (for experiments with ignition delay).

3.2. H_2/O_2 Chemical Kinetic Mechanism (Li et al.) [83]

3.2.1. Overview

Li et al. [83] attempts to create a revised model of the mechanism developed in Mueller et al. [84], and validate it against a broad range of experimental conditions, which include laminar premixed flames. The model is found to be in agreement with experimental results published subsequent to Mueller et al. [84], especially those of high-pressure laminar flame speed results. The mechanism contains 4 chain reactions, and 4 dissociation/recombination reactions for hydrogen and oxygen, and a further 11 reactions of HO_2 and H_2O_2 , amounting to a total of 19 reversible reactions. While these reactions also have the option to include inert gases such as helium and argon, there are no reactions involving

nitrogen, and subsequently, no reactions to predict the formation of NO_x . However, it was possible to use a separate NO_x module by integration from one of the other hydrogen combustion mechanisms, and therefore, the Sandiego [85] NO_x module was chosen. As the experimental conditions mentioned above are very similar to the experimental conditions in Porcarelli et al. [35], the mechanism, combined with the Sandiego NO_x module [85], could potentially be used to predict NO_x emissions numerically.

3.2.2. Validation Data

Planke et al. [82] asserts that the Li et al. mechanism has applicability for laminar premixed hydrogen flames for a temperature range of 298 - 3000K, for equivalence ratios in the range of 0.25 - 5.0, and for a pressure range of 0.3 - 87 bar.

3.3. San Diego Chemical Kinetic Mechanism [85]

3.3.1. Overview

The San Diego mechanism emphasizes the chemistry relevant to flames, high-temperature ignition, and detonations. It adopts a systematic approach, starting with simple chemical systems and progressing to more complex ones while minimising the number of species and reactions to essential components. Unlike databases seeking completeness, it prioritises a minimalist representation to reduce uncertainties in rate parameters. This approach highlights the critical importance of a small number of elementary steps' rate parameters over cumulative effects from numerous steps, contributing to more reliable predictions. Additionally, versions of this mechanism also include nitrogen chemistry, and can therefore predict NO_x emissions that result from a flame.

3.3.2. Validation Data

While no explicit temperature or pressure range is given, Paykani et al. [86] asserts that the mechanism has been validated for hydrogen combustion with experimental data.

3.4. Capurso et al. Chemical Kinetic Mechanism [87]

3.4.1. Overview

Capurso et al. [87] attempts to create a kinetic mechanism with "15 species and 47 reactions" to ensure that every NO_x formation pathway is considered for hydrogen combustion. The mechanism is specifically meant for accurate NO_x emission predictions of Large Eddy Simulations (LES) of pure hydrogen-air swirling flames..

3.4.2. Validation Data

Capurso et al. [87] validates the mechanism against a wide variety of diffusion and premixed flames from literature including "experiments performed on laminar diffusion flames at a Reynolds number of 400 diluted with inert at a constant strain rate". The NO_x module is also validated against global NO_x data from experiments.

3.5. Implications for Thesis Methodology

Several combustion mechanisms were considered for this study, including GRI-Mech 3.0 and others specifically validated for hydrogen combustion. While the latter mechanisms demonstrate better agreement with experimental data for hydrogen flames, particularly showing significant reductions in NO_x emissions at higher strain rates, GRI-Mech 3.0 was ultimately chosen. Despite being only partially validated for stoichiometric hydrogen-air combustion and under-predicting the reduction in NO_x compared to other mechanisms, its conservative estimation of NO_x emissions is a critical factor in its selection. This conservative approach ensures that the model does not underestimate the environmental impact in terms of NO_x production, aligning with the objectives of this study.

4

Methodology

4.1. Governing Equations

The equations that describe the transport processes in combustion flows encompass the Navier-Stokes equations alongside the equations for species and energy transport. The compressible transport processes pertaining to mass and momentum are specified in equations 4.1 [88] and 4.2 [88].

$$\frac{\partial}{\partial t}\rho + \frac{\partial}{\partial x_i}\rho u_i = S \quad (4.1)$$

$$\frac{\partial}{\partial t}\rho u_i + \frac{\partial}{\partial x_j}\rho u_i u_j = -\frac{\partial P}{\partial x_i} + \frac{\partial \sigma_{ij}}{\partial x_j} + S_i \quad (4.2)$$

The viscous stress tensor for the compressible momentum equation is given by equation 4.3 [88].

$$\sigma_{ij} = \mu_t \left(\frac{\partial u_i}{\partial x_j} + \frac{\partial u_j}{\partial x_i} \right) - \frac{2}{3}\mu_t \left(\frac{\partial u_k}{\partial x_k} \delta_{ij} \right) \quad (4.3)$$

The compressible equation pertaining to energy is detailed in equation 4.4.

$$\frac{\partial}{\partial t}\rho e + \frac{\partial}{\partial x_j}\rho e u_j = -P\frac{\partial u_j}{\partial x_j} + \frac{\partial}{\partial x_j} \left(K \frac{\partial T}{\partial x_j} \right) + \sigma_{ij} \frac{\partial u_i}{\partial x_j} + \frac{\partial}{\partial x_j} \left(\rho \sum_m D_m h_m \frac{\partial Y_m}{\partial x_j} \right) + S \quad (4.4)$$

Finally, the compressible equation pertaining to the conservation of species is detailed in equation 4.5.

$$\frac{\partial \rho_m}{\partial t} + \frac{\partial \rho_m u_j}{\partial x_j} = \frac{\partial}{\partial x_j} \left(\rho D_m \frac{\partial Y_m}{\partial x_j} \right) + S_m \quad \text{where} \quad \rho_m = Y_m \rho \quad (4.5)$$

In all of the above equations, D_m denotes the species specific mass diffusion coefficient, m denotes the species, e denotes the specific internal energy, h_m denotes the species specific enthalpy, K denotes the conductivity, P denotes the pressure, S denotes the source term, μ denotes the viscosity, μ' denotes the dilatational viscosity (set to zero), δ_{ij} denotes the Kronecker delta, Y_m denotes the species specific mass fraction of species m , ρ denotes the density, and u denotes the velocity. S_m is a source term that accounts for the formation or annihilation of species m , through processes such as vaporisation, chemical reactions such as combustion, and other submodels. As the mixture-averaged diffusion model was chosen for the simulations performed in this project, the local mixture-averaged diffusion coefficient is detailed by equation 4.6.

$$D_m = \frac{1 - X_m}{\sum_{j,j \neq m} \frac{X_j}{D_{mj}}} \quad (4.6)$$

In this context, X_m denotes the species specific mole fraction, while D_{mj} denotes the binary diffusion coefficient between species m and j . The expression of the binary diffusion coefficient is provided in equation 4.7 as a function of temperature and pressure.

$$D_{mj} = \frac{3}{16} \frac{\sqrt{2\pi k_B^3 T^3 / m_{mj}}}{P \pi \sigma_{mj}^2 \Omega^{(1,1)*}} \quad (4.7)$$

In which k_B is Boltzmann's constant. Hirschfelder et al.'s methodology [89] is used to compute the reduced molecular mass m_{mj} , the reduced collision diameter σ_{mj} , and the collision integral $\Omega^{(1,1)*}$ using the diffusion parameters provided in the transport.dat file.

4.2. Solver Parameters

The density-based formulation of the Pressure Implicit with Splitting of Operator (PISO) Method / Algorithm [90] was selected as the Navier Stokes solver. The algorithm starts with a predictor step where the momentum equation is resolved, followed by a correction of the pressure that is applied back to the momentum equation. The correction procedure is iterated until the specified accuracy is achieved. Once the initial pressure and momentum corrections are completed, the remaining transport equations are resolved sequentially. During the initial iteration of the PISO method, both momentum and pressure are solved, which establishes a velocity field for subsequent equations. For compressible cases, convergence is achieved when the density change $\Delta\rho$ is below a specified tolerance. A default flux blending fraction of 0.5 (second order central scheme) is selected for the momentum, species, energy, density, and passives, and 1.0 (first order upwind scheme) is selected for the turbulence. The Legacy Rhie-Chow interpolation scheme is used to couple the velocity and pressure solutions to reduce the checkerboarding effect.

4.3. Combustion Model

The SAGE detailed chemical kinetics solver [91] was selected as the combustion model. It solves the reaction rates of the many elementary reactions that can be used to describe the overall combustion reaction of hydrogen at a constant given pressure. A chemical reaction consisting of multiple steps can be written as equation 4.8 [92].



In which, for reaction i , $v'_{m,i}$ and $v''_{m,i}$ represent the coefficients of stoichiometry of species m as reactants and products, respectively. M and I denote the total number of species and reactions respectively, χ_m refers to the chemical notation of species m . The overall rate of creation of species m is defined in 4.9 [92].

$$\dot{\omega}_m = \sum_{i=1}^I v_{m,i} \cdot q_i \quad \text{where} \quad m = 1, \dots, M \quad (4.9)$$

In which q_i is the progress rate parameter for reaction i defined in equation 4.11 and $v_{m,i}$ represents the difference in stoichiometric coefficients of species m between its roles as a reactant and as a product, defined in equation 4.10 [92].

$$v_{m,i} = v''_{m,i} - v'_{m,i} \quad (4.10)$$

$$q_i = k_{f,i} \prod_{m=1}^M [X_m]^{v'_{m,i}} - k_{r,i} \prod_{m=1}^M [X_m]^{v''_{m,i}} \quad (4.11)$$

In which $[X_m]$ is the concentration in moles of species m , $k_{f,i}$ is the forward and $k_{r,i}$ is the reverse rate coefficient for reaction i respectively. The forward rate coefficient is defined in equation 4.12.

$$k_{f,i} = AT^\beta \exp\left(\frac{-E}{RT}\right) \quad (4.12)$$

In which A is the Arrhenius factor, β is the fitted rate constant, E represents the activation energy in calories per mole, T is the temperature, and R is the ideal gas constant. There are two methods to calculate the reverse rate coefficient, namely, through equation 4.12, or using the equilibrium constant $K_{c,i}$ as shown in 4.13.

$$k_{r,i} = \frac{k_{f,i}}{K_{c,i}} \quad \text{where} \quad K_{c,i} = K_{p,i} \left(\frac{P_{atm}}{RT}\right)^{\sum_{m=1}^M v_{m,i}} \quad \text{and} \quad K_{p,i} = \exp\left(\frac{\Delta S_i^0}{R} - \frac{\Delta H_i^0}{RT}\right) \quad (4.13)$$

In which P_{atm} is the atmospheric pressure, and ΔS_i^0 and ΔH_i^0 represent the change in entropy and enthalpy associated with the complete conversion of reactants to products in the i -th reaction. This allows for the solving of the fundamental equations governing the conservation of mass and energy at a given constant pressure (shown in equation 4.14 and 4.15 respectively) for a given cell in a mesh.

$$\frac{d[X_m]}{dt} = \dot{\omega}_m \quad (4.14)$$

$$\frac{dT}{dt} = \frac{\sum_m \bar{h}_m \dot{\omega}_m}{\sum_m [X_m] \bar{c}_{p,m}} \quad (4.15)$$

In which \bar{h}_m and $\bar{c}_{p,m}$ are molar and species specific enthalpy and heat capacity at a constant pressure respectively. The change in temperature obtained from equation 4.15 updates the rate coefficients in the SAGE solver. The temperature of the cell is only updated after a converged solution of the detailed chemistry is obtained using the calculated concentration of species.

4.4. Strained Counterflow Reactants-to-Products Configuration

The strained flame counterflow reactants-to-products configuration was borrowed from the study by Porcarelli et al. [35], in which a two-dimensional setup with a domain of 2 cm by 2 cm was created in OpenFOAM [93]. The same setup is replicated in ConvergeCFD (as shown in figure 4.1), with increasing levels of mesh refinement at closer proximities to the flame-front. The hydrogen combustion process was analysed under atmospheric pressure conditions (101325 Pa), and at a lean equivalence ratio of 0.7. The reactant and product temperatures were set to 300 K and 2021 K (corresponding to

the adiabatic temperature of a freely propagating premixed hydrogen flame at an equivalence ratio of 0.7 through GRI-Mech 3.0) respectively. The boundary conditions for temperature and species at the inlet reactant and product interfaces are specified as shown in table 4.1. The atmospheric pressure is specified at the outlet boundary condition.

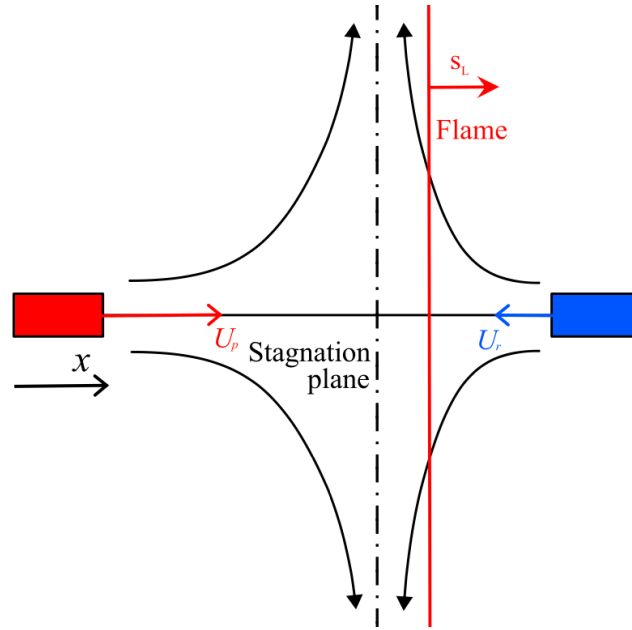


Figure 4.1: Counter-flow Reactants-to-Products Setup from Porcarelli et al. [35]

Variable Quantity	Reactants Inflow Boundary Condition	Products Inflow Boundary Condition
Temperature (T) [K]	300	2021
Hydrogen Mass Fraction (Y_{H_2}) [-]	0.02	0.00
Water Mass Fraction (Y_{H_2O}) [-]	0.00	0.18
Nitrogen Mass Fraction (Y_{N_2}) [-]	0.752	0.752
Oxygen Mass Fraction (Y_{O_2}) [-]	0.228	0.068

Table 4.1: Inlet Boundary Conditions for Domain

The inlet velocities at both the products and reactants inlet are calculated from the definition and value of the strain rate. The applied or local strain rate (a) is defined by the velocity gradient specified in equation 4.16 at the products inlet boundary [35, 64], which is used for calculating the inlet velocities of the reactants and products in this study.

$$a = \left(\frac{du_x}{dx} \right)_p \quad (4.16)$$

There also exists a definition for the global strain rate, which is defined by equation 4.17, in which u_r and u_p are the velocities prescribed at the inlets of the reactants and the products respectively, and L is the distance between the two inlets [64]. However, in this study, only the applied strain rate was used.

$$a = \frac{|u_r| + |u_p|}{L} \quad (4.17)$$

The values of the applied strain rate are specified in CHEM1D, which then calculates the inlet velocities for the reactants and products inlet boundary, as shown in table 4.2. Strain rates of $2000s^{-1}$ and $4000s^{-1}$ were selected for analysis in this study, as they not only closely align with the values used by Porcarelli et al. [35], but also provide an opportunity to assess the effect of doubling the strain rate on the flame.

Applied Strain Rate (a) [s^{-1}]	Reactants Inflow Velocity (u_r)[m/s]	Products Inflow Velocity (u_p)[m/s]
2000	-5.31	21.85
4000	-13.02	43.57

Table 4.2: Inlet Boundary Velocities

The base grid for the mesh was selected to be 0.2 by 0.2 mm. This is a departure from the mesh used by Porcarelli et al. [35], in which a base mesh size of 0.2 by 0.5 mm was used (with the longer mesh length in the y-direction). This change was mainly implemented because greater preferential diffusion was observed in the x-direction compared to the y-direction of the domain when the base mesh sizes in the x- and y-directions were shown to vary greatly.

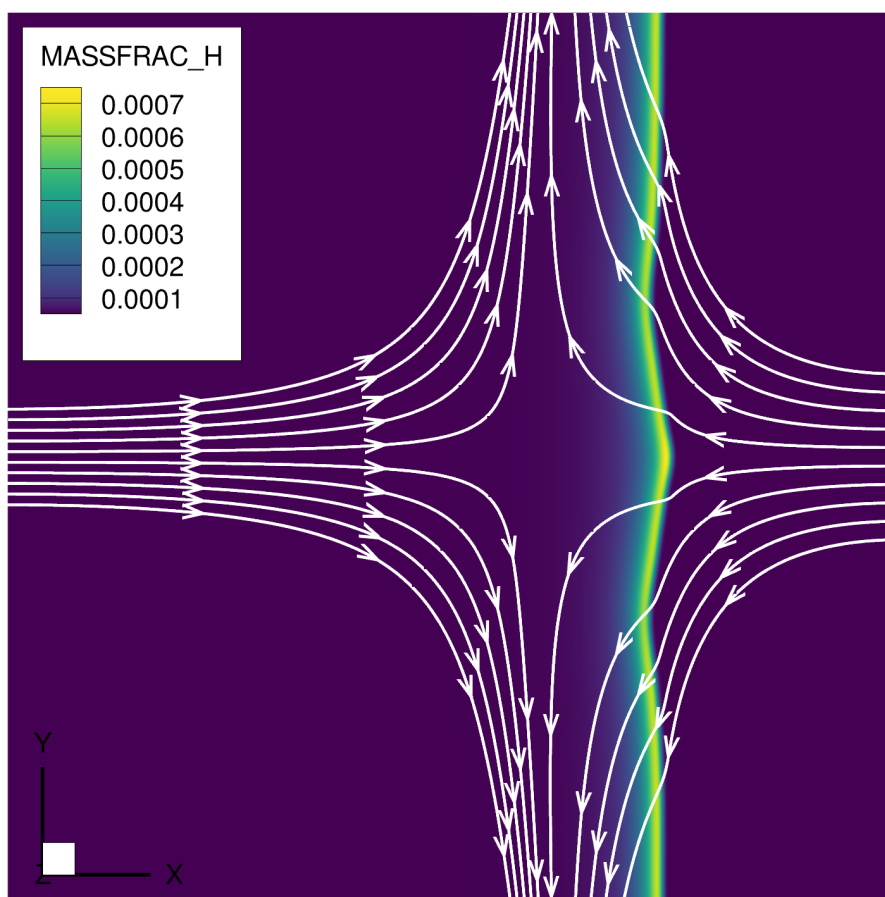


Figure 4.2: Preferential Diffusion due to Uneven Mesh Size

An occurrence of this phenomenon is shown in figure 4.2, in which the hydrogen radical mass fraction is plotted across the domain. In this figure, the flame front curves towards the inlet of the reactants near the stagnation plane, resulting in a deformed planar (U shaped) flame. The increasing levels of mesh refinement were performed through fixed embedding which decreased the size of the mesh relative to

the base grid using equation 4.18. The embedding with the scales in the domain are shown in figure 4.3.

$$\text{Embedded Grid} = \frac{\text{Base Grid}}{2^{\text{Scale}}} \quad (4.18)$$

The fixed embedding used for mesh refinement increased at least to a scale of 3 near the flame front to fully resolve the laminar flame with at least 12 cells across the laminar flame thickness for all strained simulations. This can be shown through a simple calculation performed in equation 4.26, in which the thickness of the strained laminar flame of the highest strain rate (4000 s^{-1}), obtained through calculations performed with the results of CHEM1D and verified with the results of ConvergeCFD, is divided by the width of the most refined mesh width. The formula for the calculation of the stretched laminar flame thickness is provided in equation 4.26.

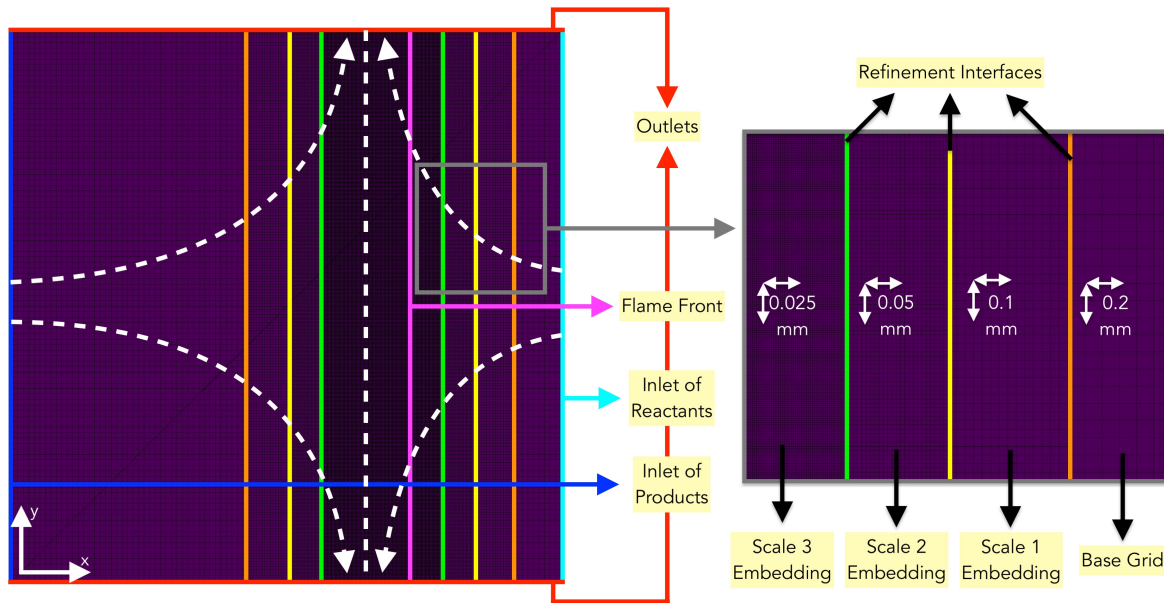


Figure 4.3: Modified Setup of Porcarelli et al. [35] in ConvergeCFD

$$\text{Cells across Laminar Flame Width} = \frac{\text{Laminar Flame Thickness}}{\text{Most Refined Mesh Width}} = \frac{0.000302}{(0.0002/2^3)} = 12.08 \quad (4.19)$$

4.5. Navier Stokes Characteristic Boundary Conditions (NSCBC)

Porcarelli et al. [35] also performed the simulations at a maximum Courant–Friedrichs–Lewy (CFL) value of 0.5, which limits the time step used in the simulation and allows the simulation to accurately capture the dynamics of the system being modelled while preventing numerical instability. To ensure that all relevant phenomena were resolved, the simulations performed in this thesis also limited the CFL number to 0.5. Furthermore, a very low Mach-based CFL number was also prescribed for the simulations (1.0) to ensure that the pressure waves generated by combustion were also fully resolved at each time step. However, this led to a strange phenomenon of the pressure field that varied drastically at each time step as shown in figure 4.4.

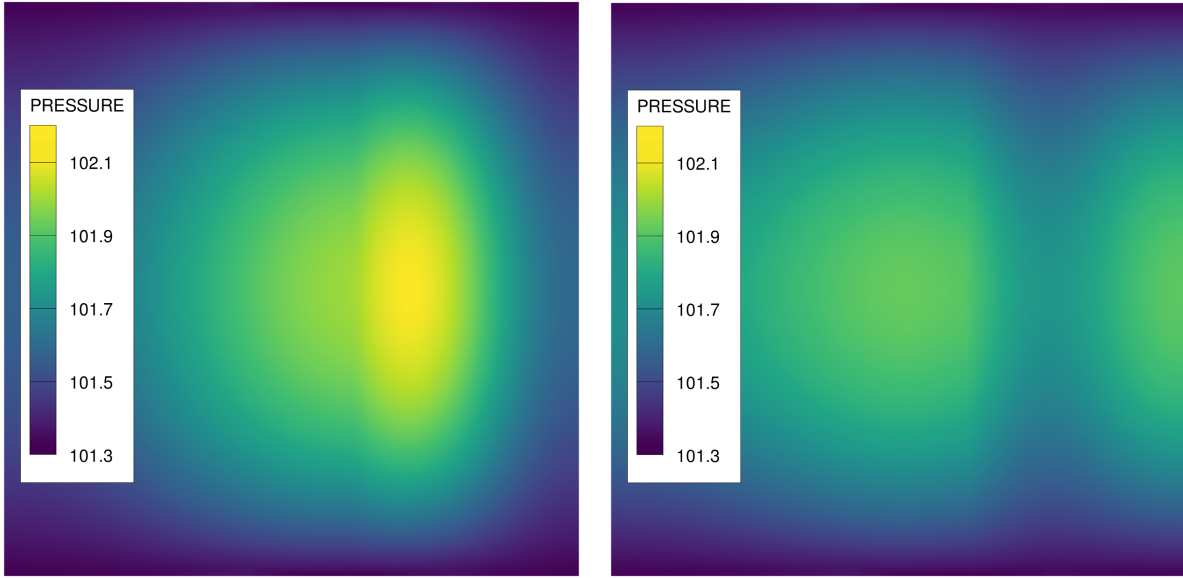


Figure 4.4: Pressure Field Fluctuating at Consecutive Time Steps

This was found to be a result of the artificially imposed Dirichlet boundary conditions that fixed the velocities at the inlets and the pressure at the outlet. As a result of the fixed pressure at the outlet boundary condition, the pressure waves were found to be reflected within the domain. The dissipation of these pressure waves did not occur sufficiently within the domain, leading to their accumulation, which would eventually create a diverging pressure large enough that led to the breakup of the flame front. Therefore, the NSCBC were used in place of the strict Dirichlet boundary conditions, allowing for the pressure waves to pass through the domain and be only partly reflected at the boundary instead of completely.

The correction-based NSCBC method [94] employs the Local One-Dimensional Incompressible (LODI) formulation to propagate waves and calculate corrections for boundary values of density, pressure, and velocity during each PISO iteration. After these corrections are computed, the boundary values for energy are reconstructed from the adjusted variables. The time evolution of the vector $U = (\rho, p, u, v, w)$, which represents the density (ρ), pressure (p), and velocity components (u, v, w), can be expressed in terms of the residual R , and where the predicted residual at iteration n is shown in equation 4.20.

$$\frac{\partial U}{\partial t} = -R \quad \text{where} \quad R^P = -\frac{U^{n+1,P} - U^n}{dt} \quad (4.20)$$

In equation 4.20, $U^{n+1,P}$ refers to the predicted (uncorrected) solution at the end of the PISO iteration. The correction-based method aims to eliminate the incoming waves present in this predicted solution and replace them with the (corrected) incoming waves that align with the specified boundary conditions. The residual is decomposed as $R = ML$, where L is the vector of wave amplitudes shown in equation 4.21 [94], and M is the matrix defined by the system of equations in equation 4.22 [94]. In these equations, c represents the speed of sound in the fluid / medium.

$$\begin{aligned}
L_1 &= \lambda_1 \left(\frac{\partial p}{\partial x} - \rho c \frac{\partial u}{\partial x} \right) & \text{where } \lambda_1 &= u - c \\
L_2 &= \lambda_2 \left(c^2 \frac{\partial \rho}{\partial x} - \frac{\partial p}{\partial x} \right) & \text{where } \lambda_2 &= u \\
L_3 &= \lambda_3 \frac{\partial v}{\partial x} & \text{where } \lambda_3 &= u \\
L_4 &= \lambda_4 \frac{\partial w}{\partial x} & \text{where } \lambda_4 &= u \\
L_5 &= \lambda_5 \left(\frac{\partial p}{\partial x} + \rho c \frac{\partial u}{\partial x} \right) & \text{where } \lambda_5 &= u + c
\end{aligned} \tag{4.21}$$

$$\begin{aligned}
\frac{\partial \rho}{\partial t} + \frac{1}{c^2} \left[L_2 + \frac{1}{2} (L_5 + L_1) \right] &= 0 \\
\frac{\partial p}{\partial t} + \frac{1}{2} (L_5 + L_1) &= 0 \\
\frac{\partial u}{\partial t} + \frac{1}{2\rho c} (L_5 - L_1) &= 0 \\
\frac{\partial v}{\partial t} + L_3 &= 0 \\
\frac{\partial w}{\partial t} + L_4 &= 0
\end{aligned} \tag{4.22}$$

The corrected solution at the boundary is calculated according to equation 4.23

$$\begin{aligned}
U^{n+1,C} &= U^n - dt \left(R^P - R_{BC}^{in,P} + R_{BC}^{in,C} \right) \\
\text{where } R_{BC}^{in,P} &= ML^{in} \quad \text{and} \quad R_{BC}^{in,C} = ML^{in,C}
\end{aligned} \tag{4.23}$$

For the correction-based method, the corrected wave amplitudes L_i^C are calculated from equation 4.24 [94]. In equation 4.24, u_∞ , v_∞ , w_∞ , T_∞ , and p_∞ correspond to the far field velocities and temperature at the inlet and the far field pressure at the outlet, specified in the boundary conditions earlier in the setup in table 4.1.

$$\begin{aligned}
\frac{\partial u}{\partial t} &= -\frac{1}{2\rho c} L_5^C = -K (u - u_\infty) \\
\frac{\partial v}{\partial t} &= -L_3^C = -K (v - v_\infty) \\
\frac{\partial w}{\partial t} &= -L_4^C = -K (w - w_\infty) \\
\frac{\partial T}{\partial t} &= -\frac{T}{\rho c^2} L_2^C = -K (T - T_\infty) \\
\frac{\partial p}{\partial t} &= -\frac{1}{2} L_1^C = -K (p - p_\infty)
\end{aligned} \tag{4.24}$$

These expressions assume that the inlet velocity and temperature relax to the far-field values with a relaxation constant K , given by equation 4.25 [94].

$$K = \sigma (1 - M^2) \frac{c}{L} \tag{4.25}$$

In equation 4.25, σ represents the under-relaxation factor, L represents the characteristic length (usually the length of the domain), M is the Mach number of the flow, and c represents the speed of sound in the fluid / medium. Although the choice of σ is highly dependent on the physics of the flow, it can usually be assumed to be 0.25 [95]. A very similar value to this (0.28) is recommended by Yoo et al. [96] and is used by Gong et al. [97] in a numerical simulation of flames with hydrogen enrichment in a real combustion chamber. Therefore, an under-relaxation factor of 0.25 and a characteristic length of 0.02 m were chosen for the inflow and outflow NSCBC.

4.6. Imposing Harmonic Perturbations to the Flame Front

Case Number	Strain Rate (a) [s^{-1}]	Amplitude of Perturbation (A_0) [-]	Wavelength of Perturbation (λ_0) [-]
Case 1	4000	0.08	4
Case 2		0.04	4
Case 3		0.08	12
Case 4		0.04	12
Case 5	2000	0.08	4
Case 6		0.04	4
Case 7		0.08	12
Case 8		0.04	12

Table 4.3: All cases investigated with varying strain rates, amplitudes, and wavelengths

Unstretched Laminar Flame Thickness ($l_{F,u}$) [mm]
0.3276

Table 4.4: Unstretched Laminar Flame Thickness of a Premixed Laminar Hydrogen Flame at an ER of 0.7

The methodology for imposing harmonic perturbations in this study follows the approach described by Berger et al. [51], where the flame front is resolved with a slightly finer mesh. In all simulation cases presented here, the flame front is resolved using a fixed embedding scale of 5 in the region near the flame. This ensures that the curvature of the imposed harmonic perturbations—likely much smaller in amplitude than the actual laminar flame thickness—are adequately captured within the simulation. The selected mesh resolution results in a minimum of 48 cells across the stretched laminar flame for all cases studied.

In contrast, the simulations performed by Berger et al. [51] employed a slightly finer mesh resolution, where the imposed perturbation amplitude of $0.04l_{F,u}$ was resolved by up to 4 cells, with a mesh resolution width of $0.01l_{F,u}$. This corresponded to over 100 cells across the unstretched laminar flame. In the present study, the smallest imposed perturbation amplitude (also $0.04l_{F,u}$) is resolved by up to 2 cells, with a mesh resolution width of $0.02l_{F,u}$. The primary reason for the slightly coarser mesh used in this study is the significantly larger computational domain, which necessitated greater computational resources to perform DNS. Increasing the mesh resolution to match that of Berger et al. [51] would have reduced the maximum allowable time step by a factor of 10 due to the constraint imposed by the CFL condition, where the maximum allowed CFL number was 0.5, for the same computational resources.

While the coarser mesh resolution used here may have resulted in incomplete resolution of the flame front curvature, potentially impacting the accuracy of the simulations, a mesh sensitivity analysis was

conducted to assess this effect. Specifically, for one case with the smallest imposed perturbation amplitude ($0.04l_{F,u}$), mesh resolutions of $0.08l_{F,u}$ and $0.04l_{F,u}$ were compared against the mesh resolution of $0.02l_{F,u}$ employed in this study. The results of this mesh sensitivity analysis are presented at the beginning of the 'Results and Analysis' section to confirm that the chosen mesh resolution provides sufficient accuracy.

The different investigated cases aim to quantify the effects of varying perturbation amplitude, perturbation wavelength, and strain rate. Therefore, the initial amplitudes and wavelengths of the imposed perturbations, as well as the applied strain rates used in the simulations, are presented in Table 4.3.

The wavelengths chosen for the simulation cases closely align with those investigated by Berger et al. [51]. A wavelength smaller than $4l_{F,u}$ was deliberately not selected, as the cutoff wavelength, where growth rates change from positive to negative, was identified by Berger et al. [51] to be between $2.3l_{F,u}$ and $3l_{F,u}$. In this range, negative growth rates would lead to the stabilisation of the flame front. Instead, the initial perturbation wavelength of $4l_{F,u}$, where $l_{F,u}$ denotes the unstretched laminar flame thickness, corresponds to initial perturbation wavelengths between $4.5l_F$ and $5.6l_F$, where l_F represents the stretched laminar flame thickness due to the imposed strain rate. These values correspond to the wavelengths that yield the highest growth rates in the simulations conducted by Berger et al. [51].

The perturbation amplitudes and wavelengths are non-dimensional values and must be multiplied by the unstretched laminar flame thickness of a premixed laminar hydrogen flame at an equivalence ratio of 0.7 to obtain the corresponding dimensional quantities. This value, determined through CHEM1D simulations and equation 4.26, is provided in Table 4.4. In this equation, T_u and T_b are the temperatures of the unburnt and burnt mixture respectively. A MATLAB code was developed to modify the MAP files obtained from ConvergeCFD after approximately 1-2 flow-through times; this code is included in the appendix. The flow through times were calculated by performing a streamline analysis of the flow in an unperturbed simulation of the flame.

$$l_F = \frac{T_b - T_u}{\max(\nabla T)} \quad (4.26)$$

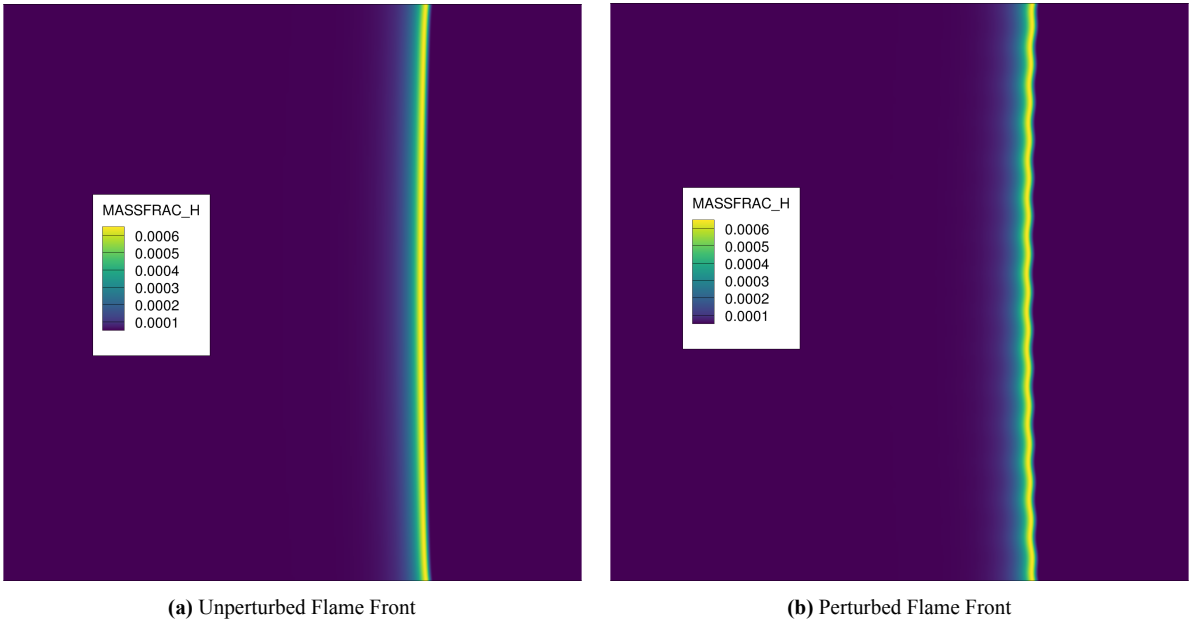


Figure 4.5: Perturbing the Flame Front

This code modifies the fields in the MAP files, $F(y)$, according to Equation 4.27, where A_0 and λ_0 represent the initial amplitude and wavelength of the perturbation, respectively, scaled by $l_{F,u}$. It is important to note that while the initial amplitude and wavelength of the imposed perturbations are scaled by the unstretched laminar flame thickness, $l_{F,u}$, the growth rates and wavenumbers presented in the results section are normalised and scaled using the stretched laminar flame thickness, l_F . An example of an unperturbed and perturbed flame front is illustrated in Figure 4.5.

$$F_{\text{modified}}(y) = A_0 \cdot l_{F,u} \cdot \cos\left(\frac{2\pi y}{\lambda_0 \cdot l_{F,u}}\right) \cdot F(y) \quad (4.27)$$

4.7. Flame Front Tracking

The tracking of the flame front is done through the progress variable of hydrogen, which is defined in equation 4.28.

$$C_{H_2} = 1 - \frac{Y_{H_2}}{Y_{H_2,u}} = 0.9 \quad (4.28)$$

In which Y_{H_2} is the mass fraction of hydrogen gas and $Y_{H_2,u}$ is the mass fraction of hydrogen gas at the unburned reactants side. Berger et al. [61, 51] find that the most reactive iso-surface of the flame front corresponds approximately to a progress variable value of 0.9 for hydrogen, which is the value of the iso-surface that is extracted from Tecplot for further analysis in the thesis. Additionally, more code is written in Matlab to track the central peak and adjacent trough of the perturbation, as shown in figure 4.6. The difference between the x-locations of the peak and trough are used to determine the amplitude of the perturbation (A) (equation 4.29), and the difference between the y-locations of the peak and trough are used to determine the wavelength (λ) of the perturbation (equation 4.30). These variables are tracked in time as the flame front evolves.

$$A = x_{\text{peak}} - x_{\text{trough}} \quad (4.29)$$

$$\lambda = 2(y_{\text{peak}} - y_{\text{trough}}) \quad (4.30)$$

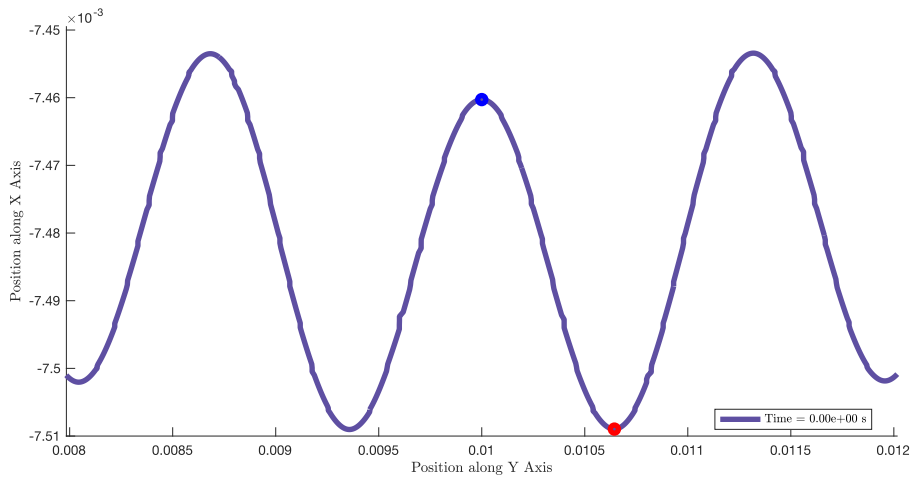


Figure 4.6: Tracking of the Central Peak and Adjacent Trough

It is also important to note that as the peak and trough closest to the center of the domain are tracked, the wavelength calculated is only representative of the wavelength of the perturbation at the center of the domain. The flame front perturbations closer to the outlet experience far greater tangential velocity gradients than the perturbations at the center of the domain, as shown by the streamlines plotted at the flame front in figure 4.7, and are, therefore, likely to vary at a different rate compared to the perturbations at the center.

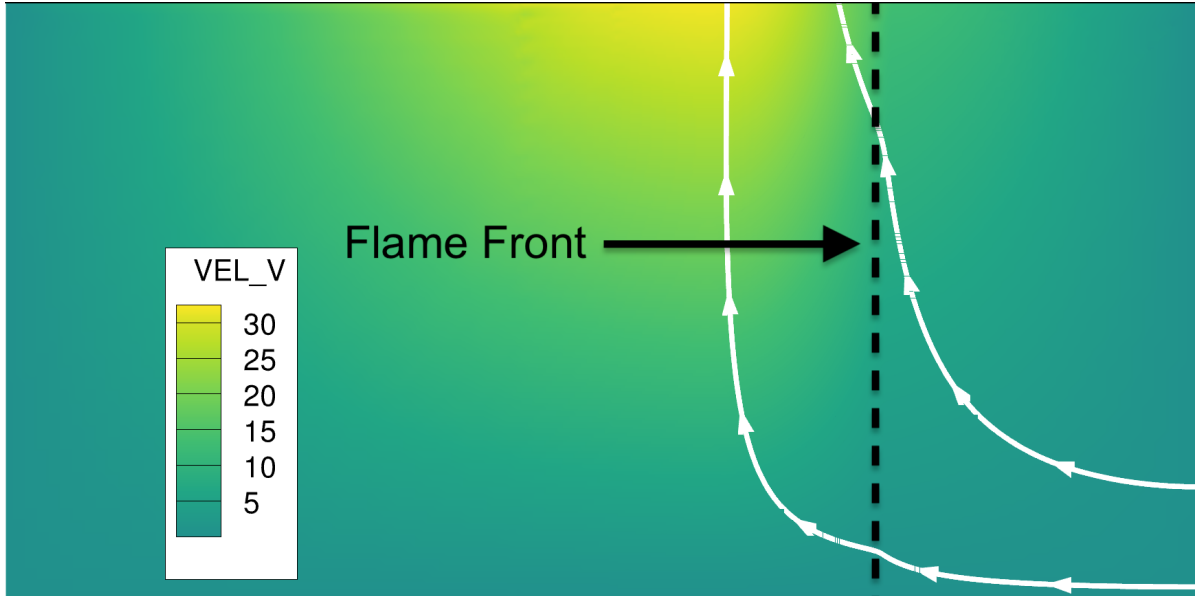


Figure 4.7: Streamlines Displaying the Tangential Velocity Gradients at the Flame Front

The growth rate (ω) of the amplitude is calculated through equation 4.31 [51].

$$\omega = \frac{d \ln A(t)}{dt} \quad (4.31)$$

In which the amplitude at time (t) = 0 seconds is set to the initial amplitude of the perturbation imposed (for example, $0.08l_F$ or $0.04l_F$). Instead of using the wavelength for the analysis, a more common approach is to plot the variation of the growth rate with the wavenumber (k) of the flame front, which can be calculated through equation 4.32 [51].

$$k(t) = \frac{2\pi}{\lambda(t)} \quad (4.32)$$

Prior to plotting the perturbation growth rates as a function of simulation time or wavenumber, it is necessary to scale these values to obtain non-dimensional quantities. This is achieved by normalising the time and spatial coordinates with respect to the flame time (τ_F) and stretched laminar flame thicknesses (l_F), respectively. These characteristic values, specific to each flame and its corresponding strain rate, are determined from CHEM1D simulations through equations ??, in which $\dot{\omega}_F$ is the fuel reaction rate in kg/s.

$$S_c = - \frac{\int \dot{\omega}_F dx}{\rho \cdot Y_{H_2,u}} \quad (4.33)$$

$$\tau_F = \frac{l_F}{S_c} \quad (4.34)$$

The resulting flame times and thicknesses for the various strain rates are summarised in Table 4.5.

Strain Rate of Flame (a) [s^{-1}]	Laminar Flame Thickness (l_F) [mm]	Flame Consumption Speed (S_c) [m/s]	Flame Time (τ_F) [ms]
0	0.328	1.14	0.288
2000	0.313	1.20	0.267
4000	0.302	1.25	0.248

Table 4.5: Stretched Laminar Flame Thicknesses and Flame Times at Varying Strain Rates

All these equations are used in the subsequent section with the results and the analysis.

Results and Analysis

This chapter contains the results of the mesh sensitivity analysis, as well as various simulations performed to observe the growth rates of the amplitudes of the perturbed flame-front simulations to determine the stabilising / destabilising nature of the strain rate on the premixed hydrogen flames.

5.1. Mesh Sensitivity Analysis

The mesh sensitivity analysis was performed for Case 6, which corresponds to the case with the smallest imposed perturbation amplitude and wavelength, analysed at a strain rate of 2000 s^{-1} .

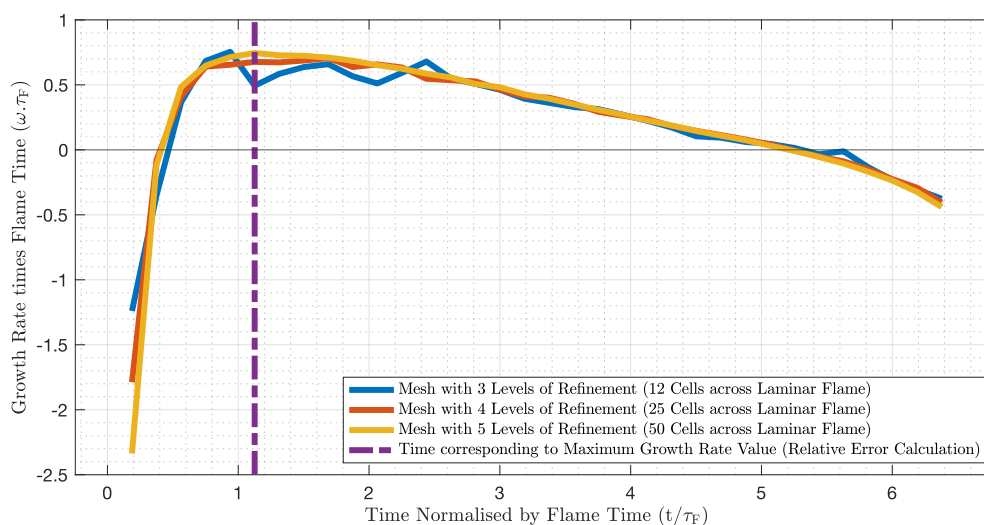


Figure 5.1: Normalised Growth Rate vs Normalised Solution Time

The normalised growth rates for varying levels of mesh refinement, scaled by the flame time, are plotted against the simulation time, also normalised by the flame time, in Figure 5.1.

The results from the mesh resolution of $0.08l_F$ (12 cells across the laminar flame) show significant deviation from the results obtained with the mesh resolution of $0.02l_F$ (50 cells across the laminar flame). This deviation is expected, as the mesh resolution width is larger than the amplitude of the imposed perturbation. Although the overall trend of the growth rate is captured, the growth rates fluctuate erratically around the results from the finer-resolution simulation, oscillating between more positive and more negative values when compared for values of the same simulation time.

For the mesh resolution of $0.04l_F$ (25 cells across the laminar flame), the results exhibit much subtler deviations, though they remain noticeable when compared to the mesh resolution of $0.02l_F$. This behaviour is also expected, given that the mesh resolution width is approximately equal to the amplitude of the imposed perturbation. The overall trend of the growth rate is captured more accurately in this case, with the variations in growth rates being much smaller relative to the finer resolution simulation when compared for values of the same simulation time.

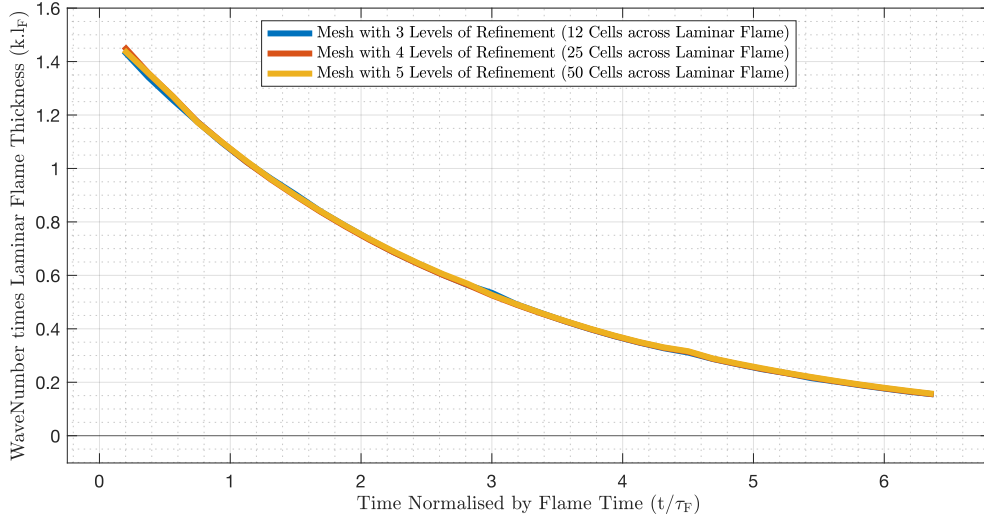


Figure 5.2: Normalised Wave Number vs Normalised Solution Time

Figure 5.2 presents the product of the wavenumber and laminar flame thickness plotted against the simulation time, normalised by the flame time. The results from all mesh resolutions are closely aligned, indicating that the variations in wavenumbers / wavelengths (due to the strain rate) are captured well across all mesh resolutions.

These observations suggest that the growth rate, which is calculated in the direction perpendicular to the flame front, is the more critical factor in determining the mesh resolution, rather than the wavenumber, which is calculated in the direction tangential to the flame front.

To quantify the accuracy of the mesh resolutions, an average relative error was computed based on the deviation of the growth rates and wavenumbers over the simulation time, following the procedure outlined in Equations 5.1 and 5.2. Furthermore, a relative error was calculated for the growth rate at the simulation time corresponding to the maximum growth rate obtained from the finest mesh resolution (shown in Figure 5.1). These error values are reported in Table 5.1.

$$\text{Relative Error Percentage} = \frac{\omega \cdot \tau_{F(\text{Low Resolution Mesh})} - \omega \cdot \tau_{F(\text{High Resolution Mesh})}}{\omega \cdot \tau_{F(\text{High Resolution Mesh})}} \cdot 100 \quad (5.1)$$

$$\text{Relative Error Percentage} = \frac{k \cdot l_{F(\text{Low Resolution Mesh})} - k \cdot l_{F(\text{High Resolution Mesh})}}{k \cdot l_{F(\text{High Resolution Mesh})}} \cdot 100 \quad (5.2)$$

The results indicate that the errors decrease from approximately 30% when comparing the 3-level refined mesh to the 5-level refined mesh, to around 8% when comparing the 4-level refined mesh to the 5-level refined mesh in terms of growth rate. This trend suggests that the most refined mesh is likely sufficient to obtain accurate results in the observed growth rates of the flame-front perturbations. Fur-

thermore, the error between the 5-level and a hypothetical 6-level refined mesh is expected to be even smaller, as evidenced by the decreasing error trends. Therefore, the increase in computational cost associated with a 6-level refined mesh is not justified, given the marginal improvement in accuracy.

Compared to Mesh with Refinement of	Relative Error at Time Corresponding to Maximum Growth Rate [%]	Average Relative Error of Growth Rates [%]	Average Relative Error of Wave Numbers [%]
3 Levels	33.7	29.7	0.7
4 Levels	9.2	8.2	0.5

Table 5.1: Relative Error Rates due to Variation in Mesh Resolution

5.2. Flame-Front Evolution for Perturbed Simulations at 4000s^{-1}

Figure 5.3 illustrates the time evolution of the flame front for Case 1. Initially, the imposed perturbations exhibit a slight increase in amplitude at the start of the simulation. This can likely be attributed to the perturbed velocity field gradually reverting to a less perturbed state, particularly near the inlets on both the reactants and products sides, where a fixed velocity is prescribed. In contrast, the wavelength of the perturbation shows a more significant growth from the outset. The increase in wavelength near the stagnation plane is relatively modest but noticeable, while a more pronounced increase occurs closer to the outlet. This difference is likely due to the lower tangential velocity gradient at the flame front near the stagnation plane center, whereas this gradient is much higher near the outlet, resulting in a greater stretch of the flame front and a corresponding change in wavelength.

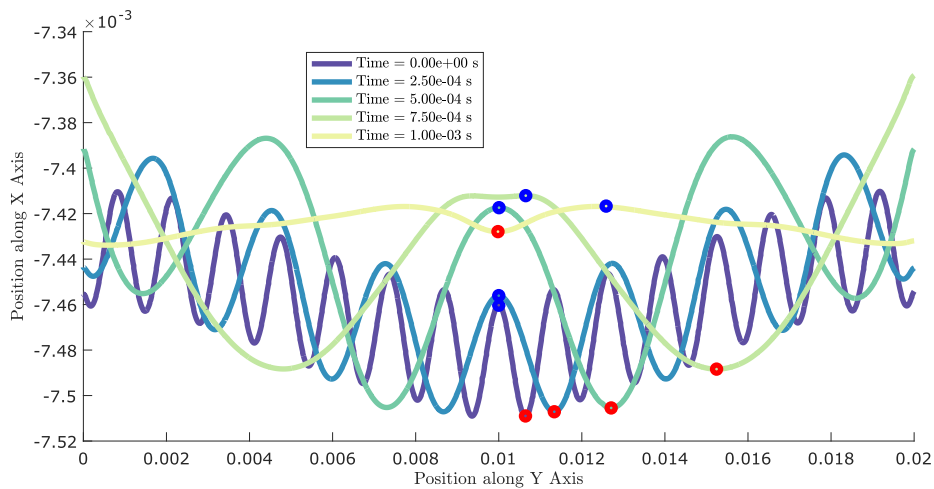


Figure 5.3: Evolution of the Flame-Front with Time (Case 1)

As time progresses, both the amplitude and wavelength of the flame front increase significantly. The amplitude growth is primarily concentrated towards the reactant inlet, where the flame front exhibits positive curvature, while the negatively curved regions remain near their original positions. At later time steps, non-harmonic effects become evident in the flame front's shape. Specifically, the central peak of the perturbed flame front begins to split into two adjacent peaks, eventually forming a central trough. In the final time step, the harmonic perturbation diminishes, leaving a nearly planar flame front with small deviations, which eventually returns to its original, unperturbed configuration.

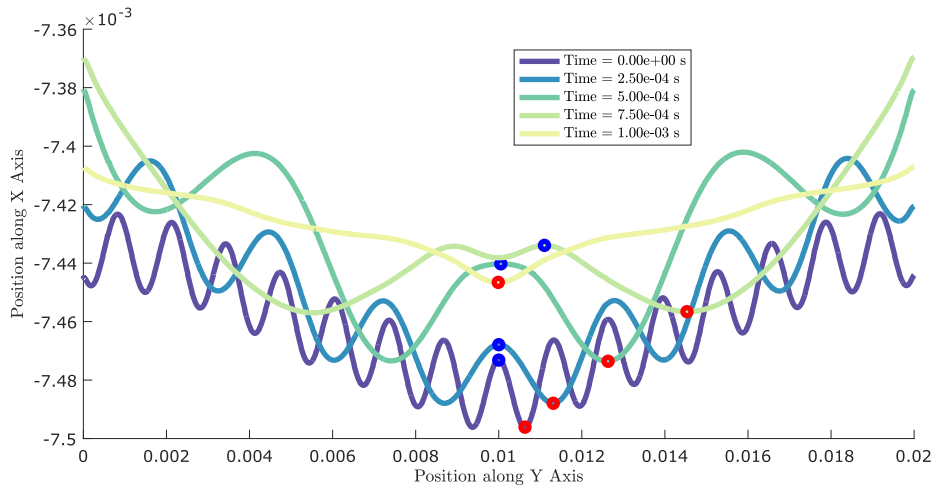


Figure 5.4: Evolution of the Flame Front with Time (Case 2)

Figure 5.4 illustrates the time evolution of the flame front for Case 2. The trends observed in Case 1 are largely applicable to Case 2, with a few notable distinctions. One key difference is that, in Case 2, both the positively and negatively curved regions of the flame front shift towards the reactant inlet, as opposed to just the positively curved regions. As the initial imposed amplitude of the perturbation for this case is half that of Case 1 and since the amplitude is defined as the difference between the x-positions of adjacent peaks and troughs, this leads to a noticeably slower growth rate of the amplitude compared to Case 1.

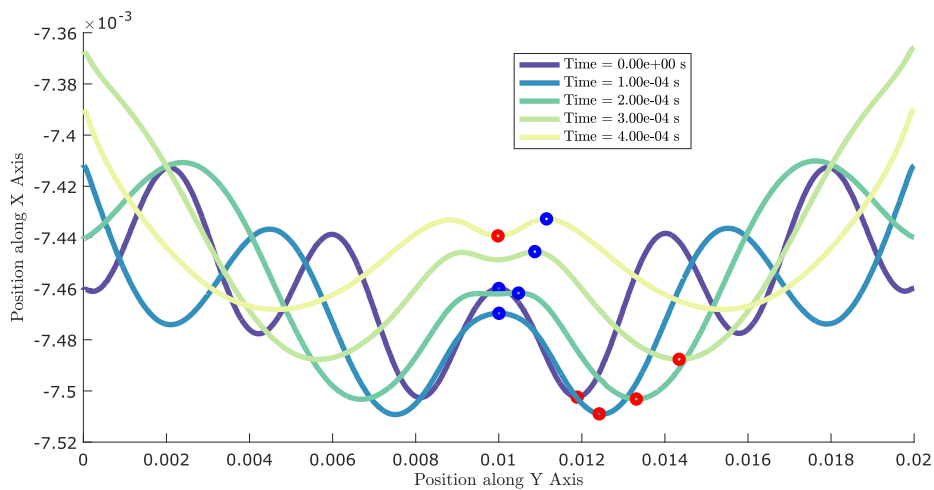


Figure 5.5: Evolution of the Flame Front with Time (Case 3)

Figure 5.5 shows the time evolution of the flame front for Case 3. Due to the significantly larger initial perturbation wavelength compared to Cases 1 and 2, the amplitude growth rate is considerably lower. Initially, the entire flame front, including both the positively and negatively curved regions, moves away from the reactant inlet towards the product inlet, before reversing direction and shifting back towards the reactant inlet. Another key difference in this case is the shorter time required for non-harmonic effects to become prominent. This is evident as the central peak splits into two at an earlier time step, even before significant amplitude growth occurs, in contrast to the behavior observed in the previous two cases.

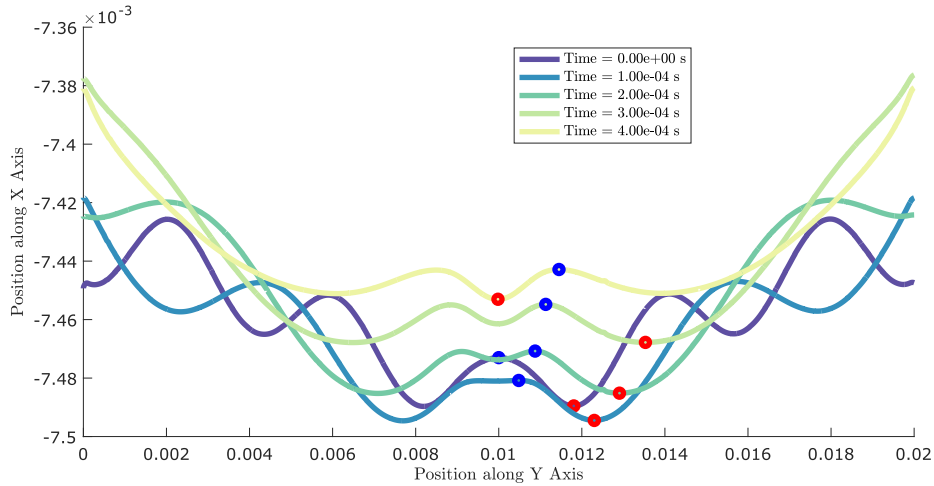


Figure 5.6: Evolution of the Flame Front with Time (Case 4)

Figure 5.6 illustrates the time evolution of the flame front for Case 4. With an initial perturbation wavelength as large as that in Case 3 but a lower initial perturbation amplitude, non-harmonic effects become evident almost immediately, even before any noticeable amplitude growth occurs. The central peak of the flame front splits into two adjacent peaks early on, as the entire front initially shifts towards the product inlet boundary. Following this, the flame front begins to reverse direction, moving towards the reactant inlet boundary.

For all high strain rate cases (4000 s^{-1}), a common feature is the splitting of the central peak of the flame front into two distinct peaks, which later evolves into a trough. This splitting is likely a consequence of the flame front moving towards the reactant inlet, driven by the higher flame consumption speed in the positively curved regions (i.e., at the peak of the perturbation). However, as the flame front progresses away from the stagnation plane, the flow velocity from the reactant side at the new flame front position becomes much higher than the flame consumption speed. This discrepancy causes the central perturbation peak to reverse direction abruptly, moving back towards the stagnation plane, leading to the appearance of peak splitting. Notably, the two newly formed adjacent peaks do not immediately reverse direction like the central peak, likely because the unperturbed flame front in this setup is slightly concave towards the reactant inlet. This concavity is likely due to the velocity gradient perpendicular to the unperturbed flame front decreasing along the y-axis, particularly as one moves away from the center.

The variation in flame consumption speed also plays a crucial role, as the cases with larger initial perturbation wavelengths display this behavior more rapidly. This can be attributed to the fact that regions with lower curvature experience a smaller increase in flame consumption speed compared to regions with higher curvature. As previously mentioned, observations have indicated that flame speed varies linearly with flame stretch, with the negative Markstein length governing this relationship. Since curvature, when multiplied by the unstretched flame speed, is a component of flame stretch, regions with higher curvature undergo a larger increase in flame stretch, and thereby, the flame consumption speed. This explains the more rapid splitting and reversal dynamics seen in cases with larger perturbation wavelengths.

5.3. Flame-Front Evolution for Perturbed Simulations at $2000s^{-1}$

Figure 5.7 depicts the temporal evolution of the flame front for Case 5. Similar to Case 1, the imposed perturbations initially exhibit a slight increase in amplitude. However, as time progresses, both the amplitude and wavelength of the flame front experience a substantial increase. The change in wavelength over the same time period is less pronounced than in Case 1, which can be attributed to the lower tangential velocity near the flame front resulting from the reduced strain rate.

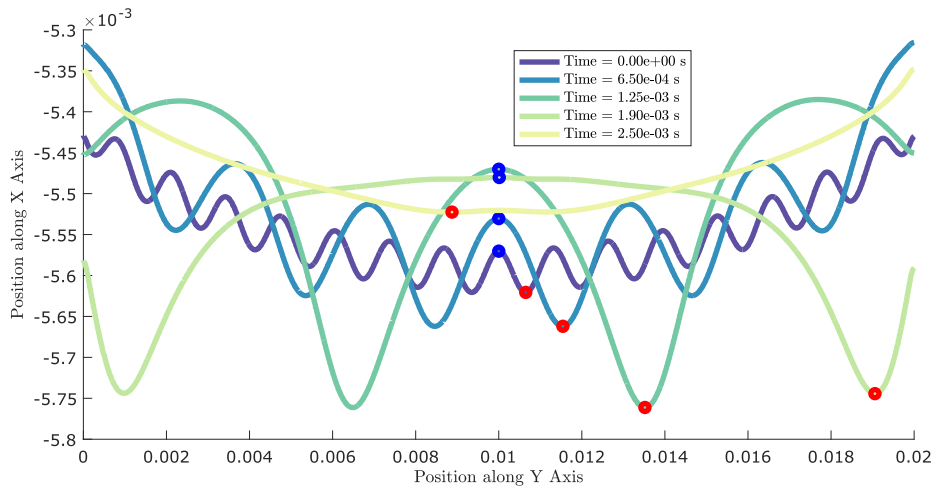


Figure 5.7: Evolution of the Flame-Front with Time (Case 5)

Notably, the growth rate appears to indicate that the amplitude of the initial perturbation in Case 5 becomes significantly larger than in Case 1. This suggests that a higher strain rate may lead to a lower or more suppressed growth rate, implying that the strain rate exerts a stabilizing influence on the flame front. Additionally, a key distinction from Case 1 is that the simulation requires a considerably longer duration for non-harmonic effects to become prominent and for the flame front to revert to its original unperturbed configuration.

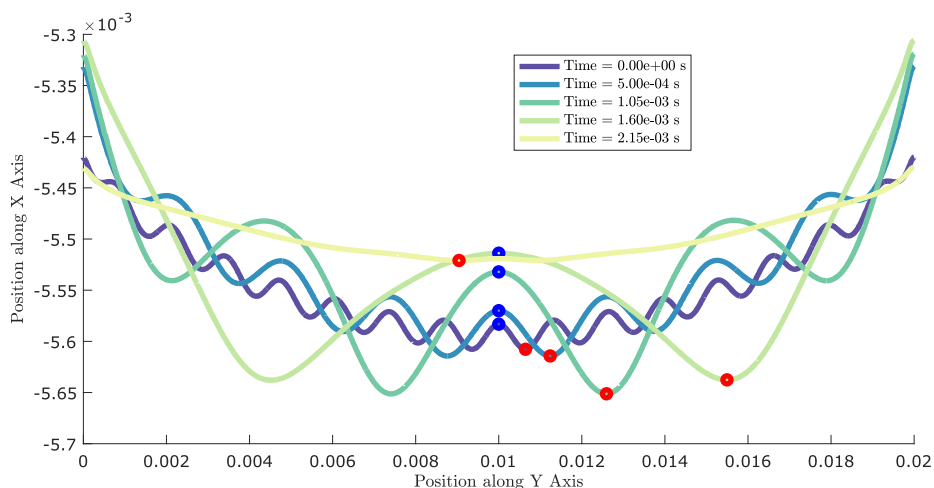


Figure 5.8: Evolution of the Flame Front with Time (Case 6)

Figure 5.8 depicts the temporal evolution of the flame front for Case 6. The trends observed in Case

5 largely apply to Case 6, with some notable differences. Specifically, the amplitude in Case 6 does not reach the same magnitude as that in Case 5, although the growth rates may be comparable due to variations in the initial perturbation amplitudes. Additionally, the simulation for Case 6 appears to require slightly less time to revert to its original unperturbed configuration.

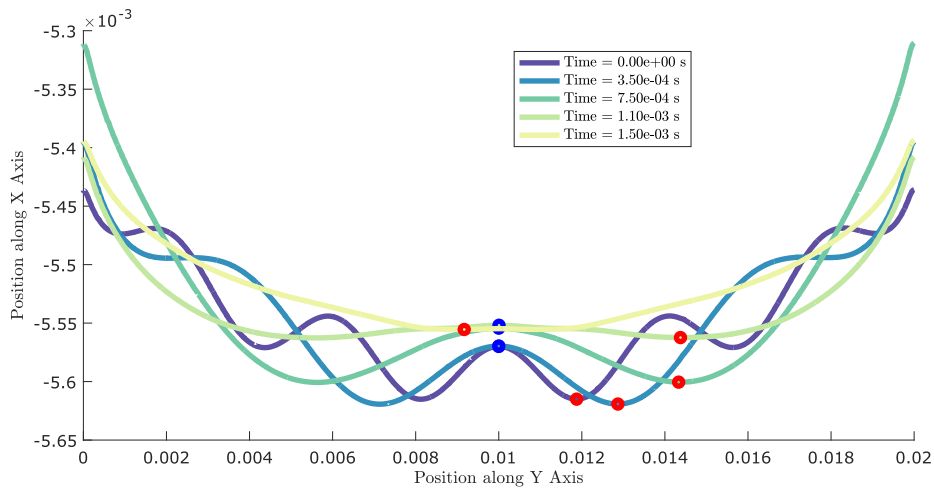


Figure 5.9: Evolution of the Flame Front with Time (Case 7)

Figure 5.9 illustrates the temporal evolution of the flame front for Case 7. Due to the significantly larger initial perturbation wavelength in this case compared to Cases 5 and 6, the amplitude growth rate is notably lower. Throughout the simulation, the central peak of the flame front perturbation exhibits minimal movement toward the reactant inlet, while the adjacent trough experiences a more pronounced displacement, initially shifting toward the product inlet and subsequently toward the reactant inlet. In contrast to Case 3, the non-harmonic effects in Case 7 take longer to manifest, and there is no splitting of the central peak into two adjacent peaks, as observed in Case 3.

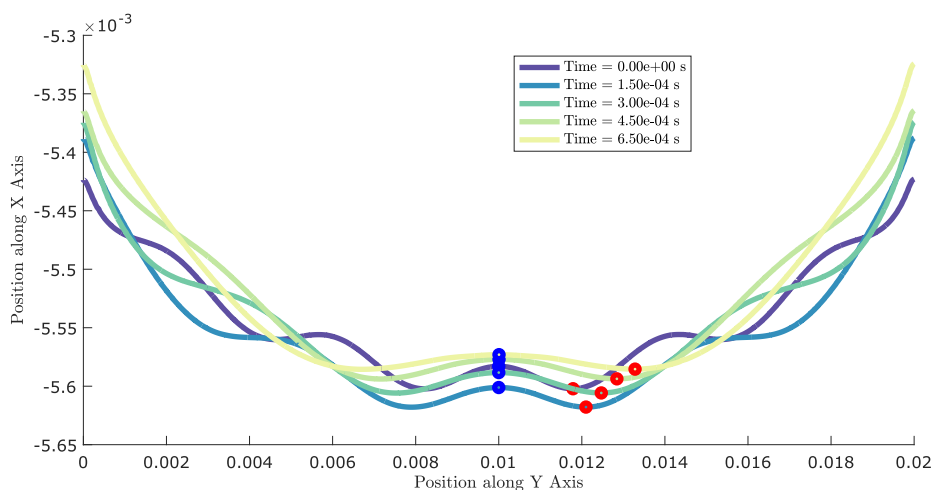


Figure 5.10: Evolution of the Flame Front with Time (Case 8)

Figure 5.10 illustrates the time evolution of the flame front for Case 8. Although the initial perturbation wavelength is the same as in Case 7, Case 8 features a lower initial perturbation amplitude. As a result, the onset of non-harmonic effects is delayed compared to Case 4, which has identical perturbation

amplitude and wavelength but operates at a higher strain rate. Unlike in Case 7, the entire flame front initially migrates toward the products inlet, a behavior also observed in Cases 3 and 4. Subsequently, the flame front shifts toward the reactants inlet and exhibits a minimal growth rate. It is possible that Case 7 also experiences an initial shift toward the products inlet; however, this is not evident in the figure due to the larger time steps employed in the plot.

For the low strain rate cases (2000 s^{-1}), the splitting of the central peak observed in high strain cases is absent. This can be attributed to the significantly lower variation in velocity perpendicular to the flame front, which is a direct result of the reduced inlet velocities of both reactants and products under the lower applied strain rate. Consequently, the flame front in these cases moves towards the reactant inlet without significant disruption. When the flame front eventually reverses direction, the tangential strain has already stretched the wavelength of the flame front's perturbations considerably, effectively flattening the flame front. As a result, the entire flame front appears to reverse direction uniformly, in contrast to the peak-splitting behavior observed in high strain cases, where increased curvature and velocity gradients lead to more localized effects.

5.4. Growth Rates for Perturbed Simulations at 4000s^{-1}

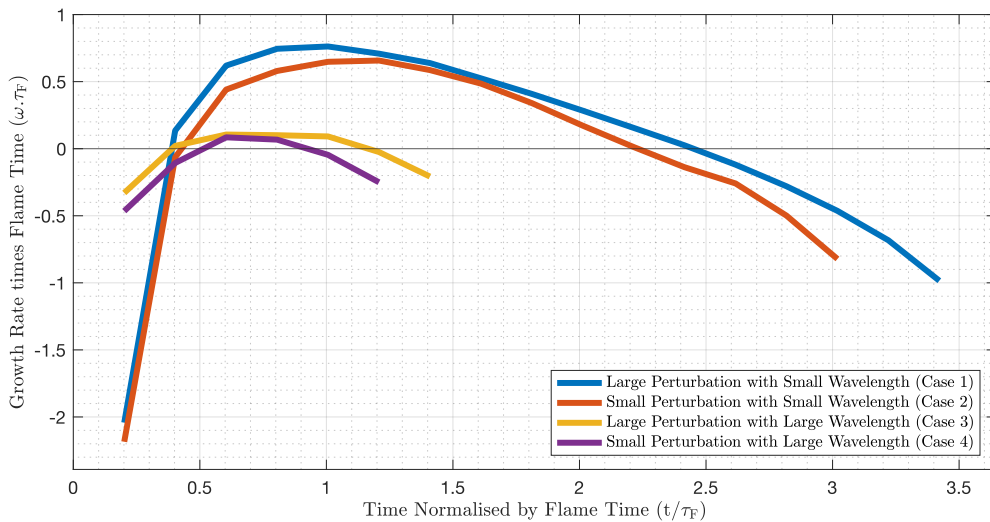


Figure 5.11: Normalised Growth Rate vs Normalised Solution Time

The normalised growth rate, scaled by the flame time, is plotted against the simulation time, also normalised by the flame time, in Figure 5.11. Cases 1 and 2 correspond to the smallest wavelength of the imposed perturbation, with differing initial perturbation amplitudes. Both cases exhibit a pronounced negative initial growth rate, which, as discussed in the previous section, arises from the perturbed velocity field returning toward a less disturbed or unperturbed state due to the boundary conditions. However, almost immediately, the growth rate shifts to positive values, reaching a maximum of approximately 0.7–0.8. These peak growth rates occur within the normalised time range of 1 to 1.5. Following this, the growth rates gradually decline and become negative once again, indicating that the flame returns to a stable configuration. The growth rate trends for both cases closely mirror one another, suggesting that the initial perturbation amplitude has a minimal effect on the growth rate evolution.

This behavior contrasts with Cases 3 and 4, where significantly larger initial wavelengths are imposed. In these cases, the initial negative growth rate is much smaller, followed by a more modest positive

growth rate within the normalised time range of 0.5 to 1. The growth rate returns to negative values much earlier in the simulation, compared to Cases 1 and 2. This indicates a more rapid stabilisation of the flame for the larger wavelength perturbations.

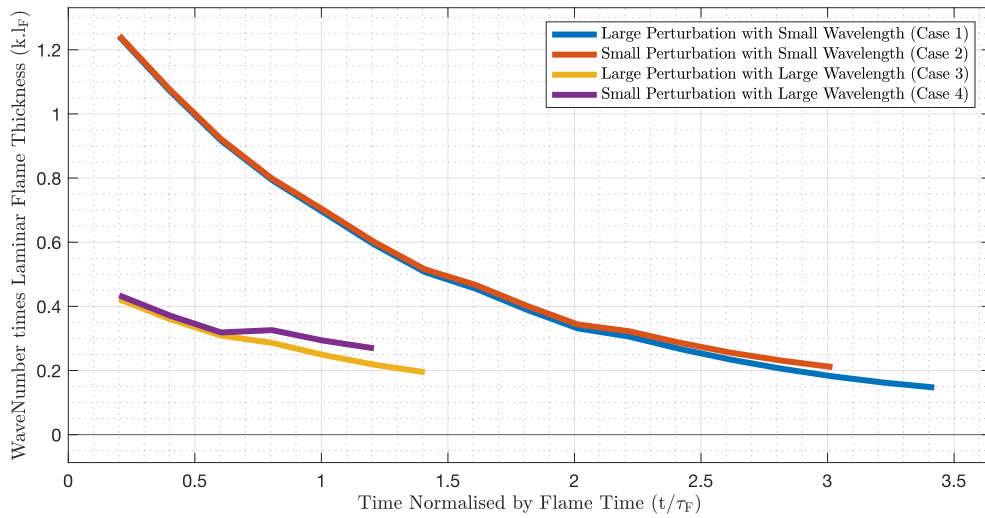


Figure 5.12: Normalised Wave Number vs Normalised Solution Time

The product of the wave number and the laminar flame thickness is plotted against the simulation time, normalised by the flame time, in Figure 5.12. In both Cases 1 and 2, the wave number initially exhibits a high value due to the small initial wavelength of the perturbation. Subsequently, the wave number decreases rapidly with simulation time. As it approaches zero, the rate of reduction diminishes, resulting in a more gradual decline. In contrast, Cases 3 and 4 begin with a lower initial wave number, leading to a slower rate of reduction. Notably, across all cases, the rate of reduction appears to be largely independent of the perturbation amplitude, instead depending predominantly on the wave number.

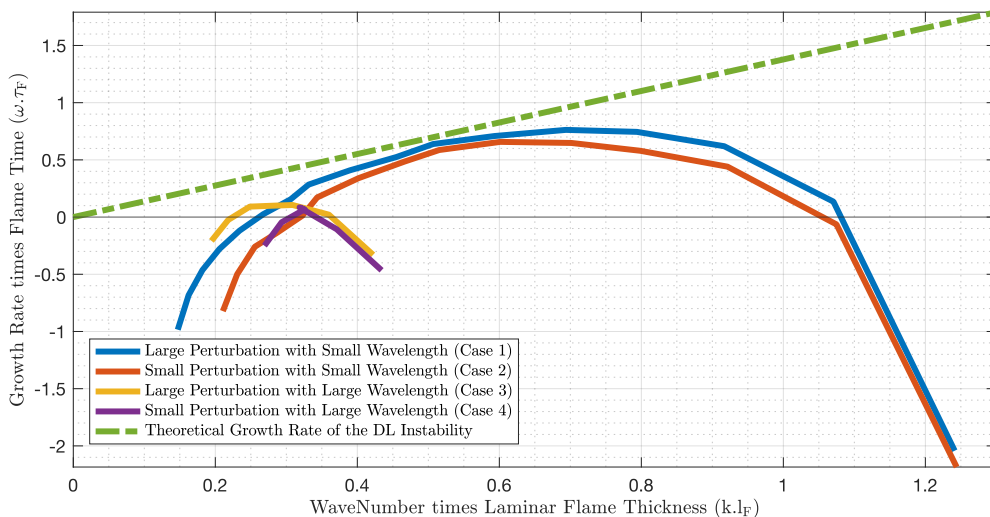


Figure 5.13: Normalised Growth Rate vs Normalised Wave Number

The normalised growth rate, scaled by the flame time, is plotted against the product of the wave number

and the laminar flame thickness in Figure 5.13. Cases 1 and 2 correspond to the largest initial wave numbers of the imposed perturbation (which are inversely related to the wavelength), with varying initial perturbation amplitudes. The maximum growth rates are observed at normalised wave number values between 0.6 and 0.8, which are significantly lower than the normalised initial wave numbers of the perturbed simulation, approximately 1.24. Following the peak, the normalised wave number continues to decrease alongside the growth rate. The growth rate values approach the theoretical predictions for the Darrieus-Landau instability at a normalised wave number of 0.5. However, throughout the simulation, the growth rate does not surpass the theoretical growth rates associated with the Darrieus-Landau instability at any normalised wave number. Eventually, at a normalised wave number of approximately 0.3, the growth rate becomes negative, indicating stabilisation of the flame and a return to its initial configuration.

5.5. Growth Rates for Perturbed Simulations at 2000s^{-1}

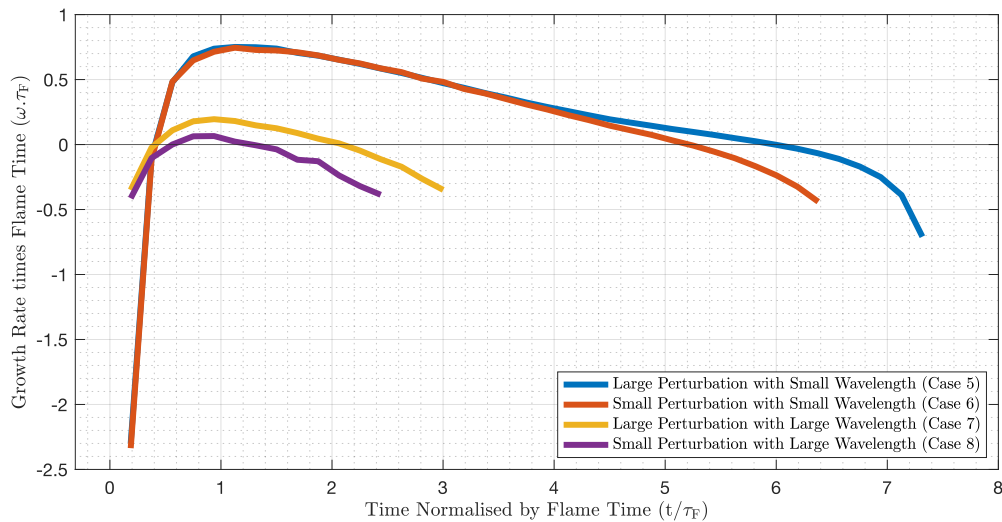


Figure 5.14: Normalised Growth Rate vs Normalised Solution Time

The normalised growth rate, scaled by the flame time, is plotted against the simulation time, which is also normalised by the flame time, in Figure 5.14. Cases 5 and 6 correspond to the smallest wavelength of the imposed perturbation, with differing initial perturbation amplitudes. Both cases exhibit a significant negative initial growth rate, akin to that observed in Cases 1 and 2. This negative growth rate arises from the perturbed velocity field returning to a less disturbed or unperturbed state due to the boundary conditions. However, almost immediately, the growth rate transitions to positive values, reaching a maximum that closely resembles the values found in Cases 1 and 2. These peak growth rates occur within the normalised time range of 1 to 1.5, suggesting that the maximum growth rate for a perturbed flame front is not significantly influenced by the increase in strain rate or the normalised time range in which it occurs.

Subsequently, the growth rates gradually decline and revert to negative values, indicating a return to a stable flame configuration. In contrast to the higher strain rate cases (Cases 1 and 2), the decline in growth rate for Cases 5 and 6 is notably slower and occurs over an extended normalised flame time, more than twice as long. This observation indicates that while the strain rate influences the rate of reduction in the growth rate, it may not affect the absolute maximum growth rate, thereby contributing

to the stabilisation of the flame front.

Similarly, Cases 7 and 8 demonstrate a small maximum growth rate associated with significantly larger initial wavelengths. In these cases, the initial negative growth rate is also reduced, followed by a more modest positive growth rate within the normalised time range of 0.8 to 1. The slight shift in the normalised flame time at which the maximum growth rate occurs may suggest a minimal, almost negligible effect of the strain rate on the maximum growth rate. Ultimately, these cases also return to a negative growth rate, albeit over a longer normalised flame time.

The longer duration for the growth rate to decrease to a negative value at lower strain rates leads to a significantly greater increase in absolute perturbation amplitude, as the growth rate reflects the exponential growth of this amplitude. In contrast, at higher strain rates, the growth rate becomes negative much more quickly, resulting in a smaller increase in absolute amplitude and, consequently, providing a stronger stabilising effect on the flame front.

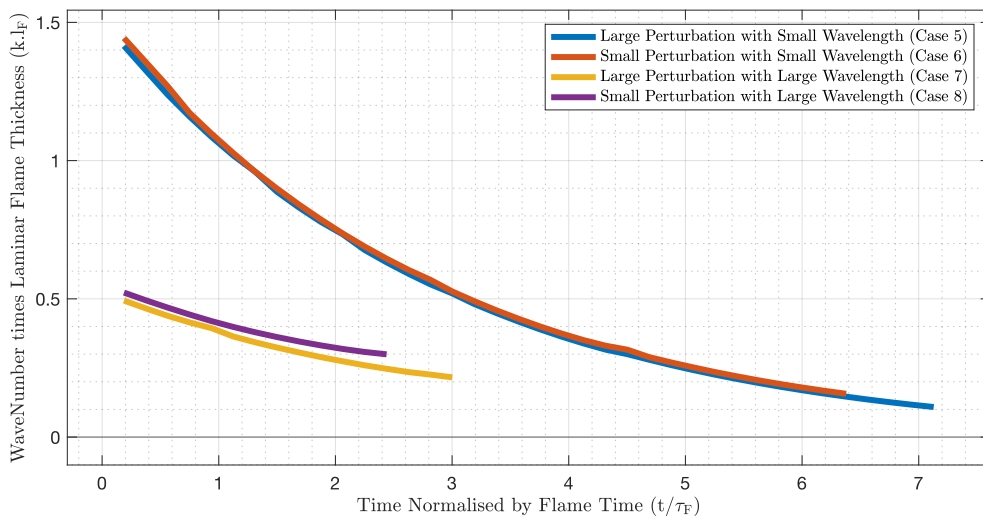


Figure 5.15: Normalised Wave Number vs Normalised Solution Time

The product of the wave number and the laminar flame thickness is plotted against the simulation time, normalised by the flame time, in Figure 5.15. As in Figure 5.12, the wave number initially exhibits a high value due to the small wavelength of the imposed perturbation. This is followed by a rapid decrease in the wave number as the simulation progresses. As the wave number approaches zero, the rate of decrease slows, resulting in a more gradual decline. The reduction in wave number appears to be primarily, if not exclusively, dependent on the initial wave number of the flame front perturbation, with negligible influence from the perturbation amplitude. At lower strain rates, where tangential velocity gradients are reduced, the wave number decreases more gradually over time compared to cases with higher strain rates.

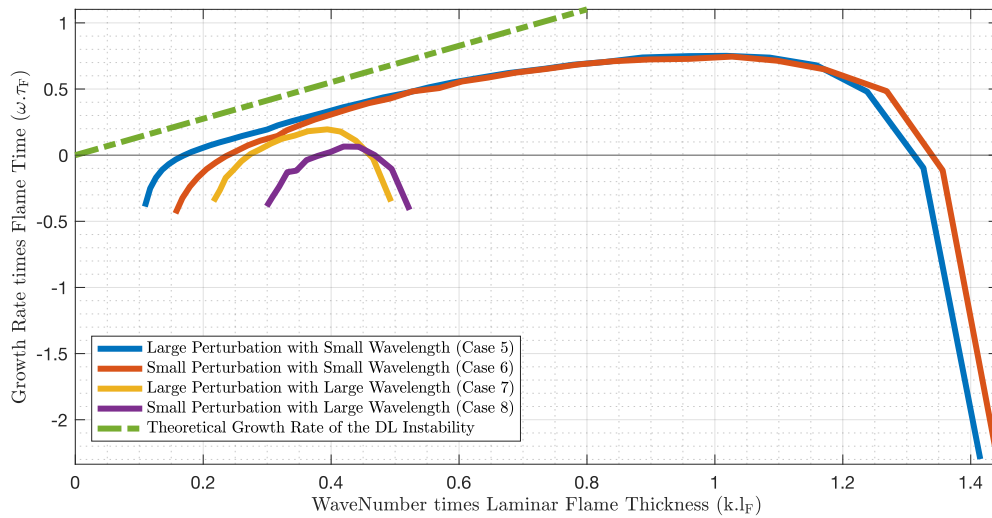


Figure 5.16: Normalised Growth Rate vs Normalised Wave Number

The normalised growth rate, scaled by the flame time, is plotted against the product of the wave number and the laminar flame thickness in Figure 5.16. Cases 5 and 6 correspond to the highest initial wave numbers of the imposed perturbation (which are inversely proportional to the wavelength) with varying initial perturbation amplitudes. The maximum growth rates occur at normalised wave number values between 0.9 and 1.1, which are significantly lower than the initial normalised wave number of approximately 1.44. After reaching the peak, both the normalised wave number and growth rate continue to decline.

Notably, the growth rate values remain substantially lower than the theoretical predictions associated with the Darrieus-Landau instability at any normalised wave number. Eventually, at a normalised wave number of around 0.2, the growth rate turns negative, signifying the stabilization of the flame and its return to the original configuration. In comparison to cases with higher strain rates, the growth rate declines more gradually, as does the decrease in wave number, owing to the less pronounced tangential velocity gradients.

5.6. Comparisons to Results from Berger et al. [51]

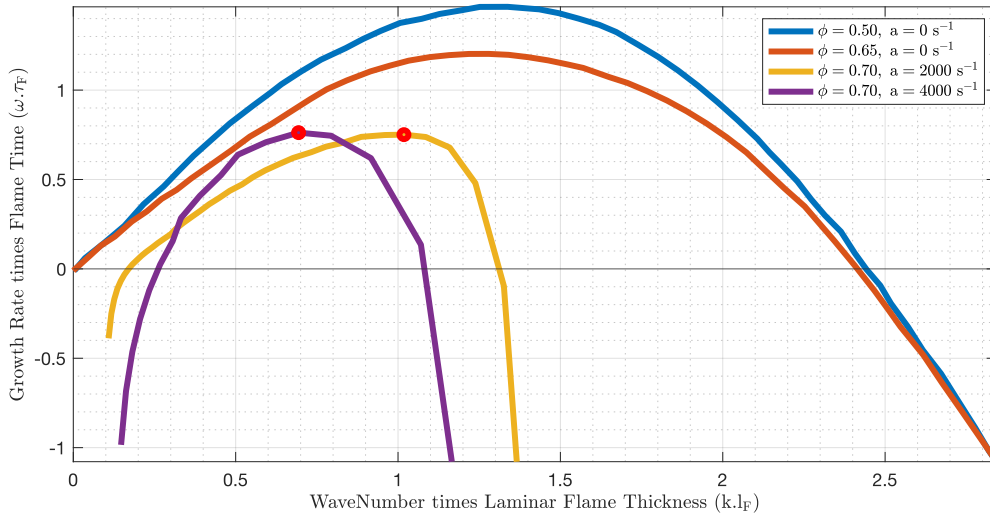


Figure 5.17: Normalised Growth Rate vs Normalised Wave Number

Figure 5.17 compares the results from Berger et al. [51] with the critical simulations from this thesis, specifically those with the largest perturbation amplitude and smallest perturbation wavelength at strain rates of 4000 s^{-1} and 2000 s^{-1} (Cases 1 and 5, respectively). The initial perturbation wave number was selected based on its correspondence to the highest growth rate observed in Berger et al.'s simulations, as shown in Figure 5.17. A higher initial wave number was avoided, as it was close to exceeding the cutoff wave number. Beyond this cutoff, the growth rate becomes negative almost immediately and remains negative throughout the simulation.

As demonstrated in the figure, the effect of increasing strain is to reduce the wave number in both simulations. Despite this, both cases reach their maximum growth rates after approximately the same normalised flame times. Although the peak growth rates are similar in magnitude for both the 2000 s^{-1} and 4000 s^{-1} strain rate cases, they occur at different wave numbers. The 4000 s^{-1} case induces a more significant reduction in the perturbation wave number compared to the 2000 s^{-1} case. However, the growth rate appears to respond more slowly to changes in the wave number (or curvature) of the perturbation, which may explain why both cases eventually reach similar maximum growth rates.

It is important to note that the results obtained in this study are not directly comparable to those presented by Berger et al. [51]. This disparity arises from the fact that multiple growth rates are observed in the graphs due to the non-linear regime in which the simulations operate (as opposed to the maximum growth rate that is plotted for each wavelength in Berger et al. [51]).

The non-linear regime in flame perturbations is characterised by whether the growth rate, defined as the time derivative of the natural logarithm of the perturbation amplitude, remains constant (linear regime) or varies significantly over time (non-linear regime). In Figure 5.18, Berger et al.'s [51] results clearly show that a constant maximum growth rate can be observed for a substantial duration (at least one flame time for the smallest wavelength), representing the linear regime. Conversely, in the simulations conducted for this study, the growth rates exhibit substantial temporal variation, indicating that the flame is in the non-linear regime.

This transition into the non-linear regime could be attributed to the variation in wavelength of the imposed perturbation, which is influenced by the tangential velocity gradients at the flame front due to the

applied tangential strain rate. However, this cannot be definitively concluded because the initial perturbation amplitudes in this study, expressed as a percentage of the unstretched laminar flame thickness, were relatively large (4% and 8%, or 4.2–4.4% and 8.4–8.8% when accounting for the stretched flame thickness). Typically, studies investigating dispersion relations in the linear regime start with smaller perturbation amplitudes, around 1–2

Interestingly, the study by Berger et al. [51] also employed a perturbation amplitude of 4% and still observed growth rates in the linear regime. This suggests that, at least for the 4% cases in this study, the transition into the non-linear regime is more likely driven by the applied strain rates rather than the high perturbation amplitudes.

Consequently, rather than identifying a single perturbation wavelength and corresponding growth rate typical of the linear regime, the current setup yields graphs that reflect these complexities. Therefore, it is important to emphasise that any comparisons made with Berger’s findings are purely illustrative, given the significant differences in the underlying conditions. Nonetheless, the primary conclusion remains that the applied tangential strain rate has a stabilising effect on the flame, which is a crucial aspect of this investigation.

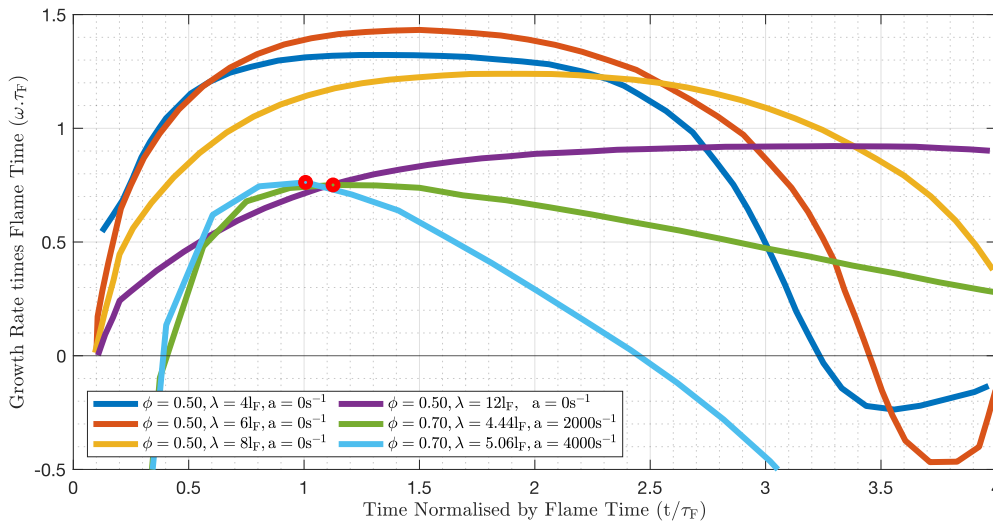


Figure 5.18: Normalised Growth Rate vs Normalised Solution Time

Figure 5.18 compares the results of the simulations conducted by Berger et al. [51] with the most critical simulations presented in this thesis, specifically Cases 1 and 5, which feature the largest perturbation amplitude and smallest perturbation wavelength at strain rates of 4000 s^{-1} and 2000 s^{-1} , respectively. It is essential to highlight the difference in equivalence ratios between the simulations from Berger et al. (0.5) and those in this thesis (0.7), as this discrepancy may influence the maximum growth rate attained in the simulations.

Both perturbed strained flames reach their maximum growth rates at approximately the same normalised flame time. However, following this peak, the simulations diverge; the growth rate of the perturbation in the 4000 s^{-1} case decreases much more rapidly than that of the 2000 s^{-1} case. If one were to connect the maximum growth rates of the reference simulations from Berger et al. across different perturbation wavelengths into a single line, it would resemble the trend observed in the strained simulations from this thesis, demonstrating that the maximum growth rate decreases with increasing perturbation wavelengths (which correspond to lower curvature).

Conclusions and Recommendations

6.1. Conclusions

6.1.1. Effects of tangential strain on the stability of perturbed laminar lean premixed hydrogen flames

The effect of the tangential strain rate on the stability of perturbed laminar lean premixed hydrogen flames is that it enhances stability. This has been consistently observed across all results, as the presence of strain rate has led to a reduction in both the maximum observed growth rate and the growth rate of the perturbation after it reaches its peak in all simulations conducted in this thesis. Furthermore, the comparison between two strain rates, 2000 s^{-1} and 4000 s^{-1} , reveals that an increase in strain rate correlates with a more rapid decline in the growth rate, leading to faster stabilisation of the flame front. The mechanism through which tangential strain influences the growth rate is via the tangential velocity gradients at the flame front. These gradients increase the total flow velocity at the flame front, particularly near the outlets, surpassing the flame consumption speed and causing the flame front to be displaced outward. This alteration in the flame front's shape reduces the effective curvature of the perturbation, subsequently decreasing its wavelength. As a result, both the maximum growth rate and the growth rates observed before and after this peak are diminished.

6.1.2. Effects of varying the amplitudes and wavelengths of the initial perturbations imposed on strained laminar lean premixed hydrogen flame fronts

The effects of varying the amplitudes and wavelengths of the initial perturbations imposed on strained flame fronts indicate that changes in the amplitude of the initial perturbation are largely insignificant regarding the maximum growth rate achieved in the simulations. In nearly all cases with differing amplitudes, while keeping other variables constant, only minor deviations in the growth rates were observed when plotted against normalised time or wave number. This trend is particularly evident in simulations with small initial wavelengths of perturbation. Conversely, in simulations featuring larger initial wavelengths, tracking the growth rates and wavelengths becomes challenging due to the rapid onset of non-harmonic effects soon after the simulation begins. However, the variation in the wavelength of the initial perturbation plays a crucial role in determining the maximum growth rate of the perturbation and influences how the growth rate evolves over time and with changing wavelengths.

6.1.3. Presence of thermoacoustic instabilities and the influence of strain rate

There are indications of thermoacoustic instabilities present in the strained hydrogen counterflow configuration, as evidenced by the reduction of the acoustic (Mach) CFL number to 0.5, which resolved all pressure waves within the domain at varying time steps. This resolution allowed pressure waves to build up, significantly influencing the unsteady heat release rate, ultimately leading to fluctuations in the pressure field and the breakup of the flame front. Notably, these phenomena were observed only in the higher strain rate cases of 4000 s^{-1} and 5000 s^{-1} , suggesting that an increase in strain rate amplifies these instabilities and inhibits the dissipation of pressure waves within the domain. Consequently, the implementation of realistic Navier-Stokes Characteristic Boundary Conditions (NSCBC) was necessary at the inlets and outlets of the domain.

6.2. Recommendations

6.2.1. Flame-Front Tracking and Wavelength Determination

While tracking the central peak and adjacent trough of the perturbation provides a method for determining its wavelength and amplitude, a more robust approach would involve assessing the wavelength through the instantaneous curvature at both the peak and the adjacent trough. This refined methodology would enhance the accuracy of wavelength determination at all points across the flame front, as the degree of curvature is primarily responsible for the growth rate observed in the simulations. By focusing on instantaneous curvature, local geometric characteristics of the flame front can be captured, which significantly influence the dynamics of flame propagation. This method would facilitate a better understanding of the relationship between curvature and growth rates, ultimately strengthening the analysis of perturbations within the strained flame environment.

6.2.2. Perturbation of All Fields except for the Velocity Field

The methodology for imposing perturbations involved modifying all fields, including species concentrations, pressure, temperature, and velocity profiles, in a sinusoidal manner. This perturbation of the velocity field resulted in an initial negative growth rate across all simulation cases at the first time step, as the velocity field returned to its unperturbed configuration due to the boundary conditions set at the inlet and outlet. While the velocity field perturbation is essential for producing a perturbed flame front in practice, it would be interesting to explore whether perturbing all other fields—excluding the velocity—would result in the velocity field naturally adjusting to match the perturbed flame front, as well as the possibly different initial growth rates of the perturbations.

A

Map File Modifying Code

```
1 clear all
2 close all
3
4 %% Specify the wavelength and amplitude of the perturbations as a function of the
   laminar flame thickness
5
6 multivar = 12;
7 % This value multiplied by the Lam_Flame_Thick gives the wavelength of the
   perturbation in meters. The values of this variable used for this project are 4
   and 12.
8
9 amplitude = 0.04;
10 % This value multiplied by the Lam_Flame_Thick gives the amplitude of the
   perturbation in meters. The values of this variable used for this project are
   0.04 and 0.08.
11
12 Lam_Flame_Thick = 0.0003276; %This is the unstretched Laminar Flame Thickness of a
   premixed hydrogen flame at an Equivalence Ratio of 0.7 in meters.
13
14 %% Specify Initial Map File Name Here
15
16 filename = 'map_1.000000e-03.h5';
17 info = h5info(filename); % This will retrieve the relevant information contained
   in the Map file.
18
19 % This for loop retrieves the names of the datasets / fields contained in the Map
   file, and assigns them to
20
21 for x = 1:28
22     Names(x) = {info(1).Groups(1).Groups(1).Datasets(x).Name};
23     ds(x) = strcat('/STREAM_00/CELL_CENTER/', Names(x));
24     currentString = Names{x};
25     Arrays{x} = h5read(filename,ds{1,x});
26     eval([currentString ' = Arrays{x};']);
27 end
28
29 SAGE_CHEM_STIFF = double(SAGE_CHEM_STIFF);
30
31 xlin = linspace(min(XCEN_X),max(XCEN_X),1000);
32 ylin = linspace(min(XCEN_Y),max(XCEN_Y),1000);
33 [X,Y] = meshgrid(xlin, ylin);
34 Z = griddata(XCEN_X,XCEN_Y,H,X,Y,'natural');
35
36 %% The following figure shows the original Hydrogen Radical Mass Fraction
37
38 figure(1)
```

```

39 hold on
40 contourf(X,Y,Z,'LineColor','none');
41 view(2)
42 axis equal
43 hold off
44
45 wavelength = multivar * Lam_Flame_Thick;
46
47 k = 2 * pi / wavelength;
48
49 A0 = amplitude * Lam_Flame_Thick;
50
51 Amplitude_X = A0 .* cos(k .* (XCEN_Y - 0.01));
52
53 F = scatteredInterpolant((Amplitude_X+XCEN_X),XCEN_Y,NO,'natural','linear');
54
55 Mod_Variable = F(XCEN_X,XCEN_Y);
56
57 Z1 = F(X,Y);
58
59 %figure(2)
60 %hold on
61 %contourf(X,Y,Z1,'LineColor','none');
62 %view(2)
63 %axis equal
64 %hold off
65
66 for i = 1:(numel(Names))-3
67     varName = Names{i}
68     modvar = eval(varName);
69     F = scatteredInterpolant((Amplitude_X+XCEN_X),XCEN_Y,modvar,'natural','linear'
70     );
71     Mod_Variable = F(XCEN_X,XCEN_Y);
72     eval([varName ' = Mod_Variable;']);
73 end
74 Z = griddata(XCEN_X,XCEN_Y,H,X,Y,'natural');
75
76 %figure(3)
77 %hold on
78 %contourf(X,Y,Z,'LineColor','none');
79 %view(2)
80 %axis equal
81 %hold off
82
83 SAGE_CHEM_STIFF = uint16(SAGE_CHEM_STIFF);
84
85 %% Specify the Initial and Modified File Names Here
86
87 copyfile map_1.000000e-03.h5 map_1.000000e-03_mod_3.h5
88
89 %% Specify the Modified File Name Here Again
90
91 filename = 'map_1.000000e-03_mod_3.h5';
92
93 tic
94 for i = 1:(numel(Names))-3
95     varName = Names{i}
96     modvar = eval(varName);
97     ds(i) = strcat('/STREAM_00/CELL_CENTER/', Names(i));
98     h5write(filename,ds{1,i},modvar)

```

```
99 end
100 toc
101
102 for x = 1:28
103     Names(x) = {info(1).Groups(1).Groups(1).Datasets(x).Name};
104     ds(x) = strcat('/STREAM_00/CELL_CENTER/', Names(x));
105     currentString = Names{x};
106     Arrays{x} = h5read(filename, ds{1,x});
107     eval([currentString '□=□Arrays{x};']);
108 end
109
110 a(1) = min(XCEN_X);
111 a(2) = max(XCEN_X);
112 a(3) = min(XCEN_Y);
113 a(4) = max(XCEN_Y);
114
115 xlin = linspace(min(XCEN_X),max(XCEN_X),1000);
116 ylin = linspace(min(XCEN_Y),max(XCEN_Y),1000);
117 [X,Y] = meshgrid(xlin, ylin);
118 Z = griddata(XCEN_X,XCEN_Y,H,X,Y,'natural');
119
120 %% The following figure shows the perturbed Hydrogen Radical Mass Fraction
121
122 figure(2)
123 hold on
124 contourf(X,Y,Z,'LineColor','none');
125 view(2)
126 axis equal
127 hold off
```

References

- [1] United Nations. *What Is Climate Change?* | United Nations — *un.org*. <https://www.un.org/en/climatechange/what-is-climate-change>. [Accessed 01-10-2024].
- [2] *Overview of Greenhouse Gases* | US EPA — *epa.gov*. <https://www.epa.gov/ghgemissions/overview-greenhouse-gases>. [Accessed 02-10-2024].
- [3] William F Ruddiman et al. “The early anthropogenic hypothesis: A review.” In: *Quaternary Science Reviews* 240 (2020), p. 106386.
- [4] Gadi Rothenberg. “A realistic look at CO₂ emissions, climate change and the role of sustainable chemistry.” In: *Sustainable Chemistry for Climate Action 2* (2023), p. 100012.
- [5] Yuyang Jiao. “Analysis of the Impacts of Carbon Dioxide Emission on Climate Change.” In: *Theoretical and Natural Science* (2023). DOI: 10.54254/2753-8818/7/20230123.
- [6] Yiming Zhao. “Technology and Advancement in Carbon Capture Based on Post-Combustion.” In: *E3s Web of Conferences* (2023). DOI: 10.1051/e3sconf/202342403006.
- [7] Richard G. Williams et al. “Sensitivity of Global Warming to Carbon Emissions: Effects of Heat and Carbon Uptake in a Suite of Earth System Models.” In: *Journal of Climate* (2017). DOI: 10.1175/jcli-d-16-0468.1.
- [8] Thomas L. Frölicher and David Paynter. “Extending the Relationship Between Global Warming and Cumulative Carbon Emissions to Multi-Millennial Timescales.” In: *Environmental Research Letters* (2015). DOI: 10.1088/1748-9326/10/7/075002.
- [9] Negar Vakilifard et al. “Assessment of Negative and Positive CO₂ Emissions on Global Warming Metrics Using Large Ensemble Earth System Model Simulations.” In: (2022). DOI: 10.5194/bg-2022-38.
- [10] Michael Moubarak et al. “Carbon Emissions and Radiative Forcings From Tundra Wildfires in the Yukon-Kuskokwim River Delta, Alaska.” In: (2022). DOI: 10.5194/bg-2022-144.
- [11] Raymond T. Pierrehumbert. “Short-Lived Climate Pollution.” In: *Annual Review of Earth and Planetary Sciences* (2014). DOI: 10.1146/annurev-earth-060313-054843.
- [12] Michael Moubarak et al. “Carbon Emissions and Radiative Forcings From Tundra Wildfires in the Yukon–Kuskokwim River Delta, Alaska.” In: *Biogeosciences* (2023). DOI: 10.5194/bg-20-1537-2023.
- [13] Yanju Chen et al. “Investigating the Linear Dependence of Direct and Indirect Radiative Forcing on Emission of Carbonaceous Aerosols in a Global Climate Model.” In: *Journal of Geophysical Research Atmospheres* (2018). DOI: 10.1002/2017jd027244.
- [14] Richard G. Williams, Paulo Ceppi, and Anna Katavouta. “Controls of the Transient Climate Response to Emissions by Physical Feedbacks, Heat Uptake and Carbon Cycling.” In: *Environmental Research Letters* (2020). DOI: 10.1088/1748-9326/ab97c9.
- [15] In: *International Civil Aviation Organisation* (Oct. 2022). URL: <https://www.icao.int/Newsroom/Pages/States-adopts-netzero-2050-aspirational-goal-for-international-flight-operations.aspx>.

- [16] Assaad R Masri. “Challenges for turbulent combustion.” In: *Proceedings of the Combustion Institute* 38.1 (2021), pp. 121–155.
- [17] *The hydrogen colour spectrum*| National Grid Group — *nationalgrid.com*. <https://www.nationalgrid.com/stories/energy-explained/hydrogen-colour-spectrum>. [Accessed 02-10-2024].
- [18] Pierre Friedlingstein et al. “Global carbon budget 2020.” In: *Earth System Science Data Discussions* 2020 (2020), pp. 1–3.
- [19] David S Lee et al. “The contribution of global aviation to anthropogenic climate forcing for 2000 to 2018.” In: *Atmospheric environment* 244 (2021), p. 117834.
- [20] Milan Klöwer et al. “Quantifying aviation’s contribution to global warming.” In: *Environmental Research Letters* 16.10 (2021), p. 104027.
- [21] Thirupathi Boningari and Panagiotis G Smirniotis. “Impact of nitrogen oxides on the environment and human health: Mn-based materials for the NOx abatement.” In: *Current Opinion in Chemical Engineering* 13 (2016), pp. 133–141.
- [22] Sebastian Verhelst and Thomas Wallner. “Hydrogen-fueled internal combustion engines.” In: *Progress in energy and combustion science* 35.6 (2009), pp. 490–527.
- [23] Etienne Rivard, Michel Trudeau, and Karim Zaghbi. “Hydrogen storage for mobility: A review.” In: *Materials* 12.12 (2019), p. 1973.
- [24] Bernard Lewis and Guenther Von Elbe. *Combustion, flames and explosions of gases*. Elsevier, 2012.
- [25] Raymond L Speth and Ahmed F Ghoniem. “Using a strained flame model to collapse dynamic mode data in a swirl-stabilized syngas combustor.” In: *Proceedings of the combustion institute* 32.2 (2009), pp. 2993–3000.
- [26] Joachim Beeckmann and Heinz Pitsch. “Laminar burning velocities of spherically expanding hydrogen/air mixtures for temperatures up to 423 k at ambient pressure.” In: *Proceedings of the twenty-sixth international colloquium on the dynamics of explosions and reactive systems*. 2017, Paper1175.
- [27] Yu-Chun Lin et al. “Turbulent Flame Speed as an Indicator for Flashback Propensity of Hydrogen-Rich Fuel Gases.” In: *Journal of Engineering for Gas Turbines and Power* (2013). DOI: 10.1115/1.4025068.
- [28] Dominik Ebi, Rolf Bombach, and P. Jansohn. “Swirl Flame Boundary Layer Flashback at Elevated Pressure: Modes of Propagation and Effect of Hydrogen Addition.” In: *Proceedings of the Combustion Institute* (2021). DOI: 10.1016/j.proci.2020.06.305.
- [29] Arvind Gangoli Rao. “Low emission combustor technology for aero engines.” In: *TU Delft* (2022).
- [30] SA Shakariyants. “Generic methods for aero-engine exhaust emission prediction.” Undefined/Unknown. Dissertation (TU Delft). Delft University of Technology, 2008. ISBN: 9789090233468.
- [31] IB Zeldovich. “Mathematical theory of combustion and explosions.” In: *Consultants Bureau* (1985).
- [32] Ya B Zeldvich. “The oxidation of nitrogen in combustion and explosions.” In: *J. Acta Physicochimica* 21 (1946), p. 577.
- [33] Song Wu et al. “NOx Emissions and Nitrogen Fate at High Temperatures in Staged Combustion.” In: *Energies* (2020). DOI: 10.3390/en13143557.

- [34] Suhani Agarwal, Pranav V. Kherdekar, and Divesh Bhatia. “Reaction Pathway Analysis for Investigation of the NO_x Reduction Mechanism During Selective NO_x Recirculation in a Hydrogen Engine.” In: *Energy & Fuels* (2022). DOI: 10.1021/acs.energyfuels.2c00411.
- [35] Alessandro Porcarelli, Boris Kruljević, and Ivan Langella. “Suppression of NO_x emissions by intensive strain in lean premixed hydrogen flamelets.” In: *International Journal of Hydrogen Energy* (2023).
- [36] Yanfei Zhang. “Effects of Hydrogen Addition, Oxygen Level, and Strain Rate on Combustion Characteristics of CH₄/H₂ in Staged MILD Combustion.” In: *Energy Technology* (2023). DOI: 10.1002/ente.202301187.
- [37] Bassam Mohammad et al. “Hydrogen Enrichment Impact on Gas Turbine Combustion Characteristics.” In: (2021). DOI: 10.1115/1.0003031v.
- [38] Shiyong Cao et al. “Numerical and Experimental Studies of NO Formation Mechanisms Under Methane Moderate or Intense Low-Oxygen Dilution (MILD) Combustion Without Heated Air.” In: *Energy & Fuels* (2015). DOI: 10.1021/ef501943v.
- [39] Mario Ditaranto, Tarjei Heggset, and David Berstad. “Concept of hydrogen fired gas turbine cycle with exhaust gas recirculation: Assessment of process performance.” In: *Energy* 192 (2020), p. 116646.
- [40] Mostafa Raafat Kotob, Tianfeng Lu, and Seddik S. Wahid. “Experimental Study of Direct Water Injection Effect on NO_x Reduction From the Gas Fuel.” In: *Journal of Advanced Research in Fluid Mechanics and Thermal Sciences* (2020). DOI: 10.37934/arfm.76.3.92108.
- [41] Haiqin Zhou et al. “Hydrogen-fueled gas turbines in future energy system.” In: *International Journal of Hydrogen Energy* 64 (2024), pp. 569–582.
- [42] H. H.-W. Funke et al. “Experimental and Numerical Study on Optimizing the DLN Micromix Hydrogen Combustion Principle for Industrial Gas Turbine Applications.” In: (2015). DOI: 10.1115/gt2015-42043.
- [43] Johannes Berger. “Scaling of an Aviation Hydrogen Micromix Injector Design for Industrial GT Combustion Applications.” In: *Aerotecnica Missili & Spazio* (2021). DOI: 10.1007/s42496-021-00091-5.
- [44] Sandeep Alavandi, Shahrokh Etemad, and Benjamin Baird. “Low Single Digit NO_x Emissions Catalytic Combustor for Advanced Hydrogen Turbines for Clean Coal Power Systems.” In: (2012). DOI: 10.1115/gt2012-68128.
- [45] Hong-juan et al. “Experimental Investigation of the Combustion Characteristics of Ammonia Addition to the Dry Low NO_x Hydrogen Combustor.” In: (2023). DOI: 10.46855/energy-proceedings-10509.
- [46] Stefano Cocchi and Stefano Sigali. “Development of a low-NO_x hydrogen-fuelled combustor for 10 MW class gas turbines.” In: *Turbo Expo: Power for Land, Sea, and Air*. Vol. 43970. 2010, pp. 1025–1035.
- [47] Alessio Pappa et al. “Can water dilution avoid flashback on a hydrogen-enriched micro-gas turbine combustion?—a large eddy simulations study.” In: *Journal of Engineering for Gas Turbines and Power* 143.4 (2021), p. 041008.
- [48] Alessandro Cappelletti and Francesco Martelli. “Investigation of a pure hydrogen fueled gas turbine burner.” In: *International Journal of Hydrogen Energy* 42.15 (2017), pp. 10513–10523.
- [49] K Inoue et al. “Development of hydrogen and natural gas co-firing gas turbine.” In: *Mitsubishi Heavy Industries Technical Review* 55.2 (2018), p. 1.

- [50] Seyed Ehsan Hosseini. *Fundamentals of low emission flameless combustion and its applications*. Academic Press, 2022.
- [51] Lukas Berger, Antonio Attili, and Heinz Pitsch. “Intrinsic instabilities in premixed hydrogen flames: Parametric variation of pressure, equivalence ratio, and temperature. part 1-dispersion relations in the linear regime.” In: *Combustion and Flame* 240 (2022), p. 111935.
- [52] Pasquale Eduardo Lapenna et al. “Hydrogen Laminar Flames.” In: *Hydrogen for Future Thermal Engines*. Springer, 2023, pp. 93–139.
- [53] Francis Oppong et al. “Intrinsic instability of different fuels spherically expanding flames: a review.” In: *Fuel Processing Technology* 234 (2022), p. 107325.
- [54] JK Bechtold and Moshe Matalon. “The dependence of the Markstein length on stoichiometry.” In: *Combustion and flame* 127.1-2 (2001), pp. 1906–1913.
- [55] J Bechtold and M Matalon. “Some new results on Markstein number predictions.” In: *38th Aerospace Sciences Meeting and Exhibit*. 2000, p. 575.
- [56] Moshe Matalon. “Combustion theory.” In: *CEFRC Summer School, Princeton University* (2011).
- [57] Moshe Matalon. “Flame dynamics.” In: *Proceedings of the Combustion Institute* 32.1 (2009), pp. 57–82.
- [58] M Matalon, C Cui, and JK Bechtold. “Hydrodynamic theory of premixed flames: effects of stoichiometry, variable transport coefficients and arbitrary reaction orders.” In: *Journal of fluid mechanics* 487 (2003), pp. 179–210.
- [59] Gregory I Sivashinsky. “Instabilities, pattern formation, and turbulence in flames.” In: (1982).
- [60] Pasquale Eduardo Lapenna et al. “Large scale effects in weakly turbulent premixed flames.” In: *Proceedings of the combustion institute* 37.2 (2019), pp. 1945–1952.
- [61] Lukas Berger et al. “Flame fingers and interactions of hydrodynamic and thermodiffusive instabilities in laminar lean hydrogen flames.” In: *Proceedings of the Combustion Institute* 39.2 (2023), pp. 1525–1534.
- [62] Lukas Berger, Antonio Attili, and Heinz Pitsch. “Synergistic interactions of thermodiffusive instabilities and turbulence in lean hydrogen flames.” In: *Combustion and Flame* 244 (2022), p. 112254.
- [63] Dan Zhao. *Thermoacoustic Combustion Instability Control: Engineering Applications and Computer Codes*. Academic Press, 2023.
- [64] Matthew X Yao. “Thermoacoustic instabilities in counterflow diffusion flames.” MA thesis. University of Waterloo, 2019.
- [65] Thierry Poinso and Denis Veynante. *Theoretical and numerical combustion*. RT Edwards, Inc., 2005.
- [66] Alexandre Ern and Vincent Giovangigli. *Multicomponent transport algorithms*. Vol. 24. Springer Science & Business Media, 1994.
- [67] A Ern and V Giovangigli. “Eglib: A general-purpose fortran library for multicomponent transport property evaluation.” In: *Manual of EGlib version 3* (2004), p. 12.
- [68] Alexandre Ern and Vincent Giovangigli. “Impact of detailed multicomponent transport on planar and counterflow hydrogen/air and methane/air flames.” In: *Combustion science and technology* 149.1-6 (1999), pp. 157–181.
- [69] Ehsan Abbasi-Atibeh and Jeffrey M Bergthorson. “The effects of differential diffusion in counterflow premixed flames with dilution and hydrogen enrichment.” In: *Combustion and Flame* 209 (2019), pp. 337–352.

- [70] Joseph F Grcar, John B Bell, and Marcus S Day. “The Soret effect in naturally propagating, premixed, lean, hydrogen–air flames.” In: *Proceedings of the Combustion Institute* 32.1 (2009), pp. 1173–1180.
- [71] Aaron J Fillo et al. “Assessing the impact of multicomponent diffusion in direct numerical simulations of premixed, high-Karlovitz, turbulent flames.” In: *Combustion and Flame* 223 (2021), pp. 216–229.
- [72] D Zhang. “Ash fouling, deposition and slagging in ultra-supercritical coal power plants.” In: *Ultra-Supercritical Coal Power Plants* (2013), pp. 133–183.
- [73] Mohammad Hemmat Esfe, Saeed Esfandeh, and Mohammad Hassan Kamyab. “History and introduction.” In: *Hybrid Nanofluids for Convection Heat Transfer*. Elsevier, 2020, pp. 1–48.
- [74] Fan Yang et al. “A mechanistic study of Soret diffusion in hydrogen–air flames.” In: *Combustion and Flame* 157.1 (2010), pp. 192–200.
- [75] Lukas Berger et al. “Characteristic patterns of thermodiffusively unstable premixed lean hydrogen flames.” In: *Proceedings of the Combustion Institute* 37.2 (2019), pp. 1879–1886.
- [76] Xu Wen et al. “Numerical analysis and flamelet modeling of NO_x formation in a thermodiffusively unstable hydrogen flame.” In: *Combustion and Flame* 253 (2023), p. 112817.
- [77] Marc S Day et al. “Numerical simulation of nitrogen oxide formation in lean premixed turbulent H₂/O₂/N₂ flames.” In: *Proceedings of the Combustion Institute* 33.1 (2011), pp. 1591–1599.
- [78] Alessandro Porcarelli and Ivan Langella. “Mitigation of preferential diffusion effects by intensive strain in lean premixed hydrogen flamelets.” In: *Submitted to the proceedings of the Combustion Institute* (2023).
- [79] Maria R Acquaviva, Alessandro Porcarelli, and Ivan Langella. “Effect of Soret diffusion on flame characteristics and NO_x emissions in highly strained lean premixed hydrogen flamelets.” In: *Submitted to the proceedings of the Combustion Institute* (2023).
- [80] Lukas Berger, Antonio Attili, and Heinz Pitsch. “Intrinsic instabilities in premixed hydrogen flames: parametric variation of pressure, equivalence ratio, and temperature. Part 2–Non-linear regime and flame speed enhancement.” In: *Combustion and Flame* 240 (2022), p. 111936.
- [81] Gregory P Smith. “GRI-Mech 3.0.” In: http://www.me.berkeley.edu/gri_mech/ (1999).
- [82] Karl Planke et al. “A Numerical Study on Hydrogen Jet Flame Combustion in MILD Conditions.” In: *AIAA SciTech 2023 Forum*. 2023, p. 1098.
- [83] Juan Li et al. “An updated comprehensive kinetic model of hydrogen combustion.” In: *International journal of chemical kinetics* 36.10 (2004), pp. 566–575.
- [84] MA Mueller et al. “Flow reactor studies and kinetic modeling of the H₂/O₂ reaction.” In: *International journal of chemical kinetics* 31.2 (1999), pp. 113–125.
- [85] FA Williams. *Chemical-kinetic mechanisms for combustion applications. San Diego mechanism web page, mechanical and aerospace engineering (combustion research), University of California at San Diego*. 2017.
- [86] Amin Paykani. “Comparative Study on Chemical Kinetics Mechanisms for Methane-Based Fuel Mixtures under Engine-Relevant Conditions.” In: *Energies* 14.10 (2021), p. 2834.
- [87] T Capurso et al. “NO_x pathways in lean partially premixed swirling H₂-air turbulent flame.” In: *Combustion and Flame* 248 (2023), p. 112581.
- [88] Jürgen Warnatz et al. “Transport Phenomena.” In: *Combustion: Physical and Chemical Fundamentals, Modeling and Simulation, Experiments, Pollutant Formation* (1999), pp. 49–64.

- [89] Joseph O Hirschfelder, Charles F Curtiss, and R Byron Bird. *The molecular theory of gases and liquids*. John Wiley & Sons, 1964.
- [90] Raad I Issa. “Solution of the implicitly discretised fluid flow equations by operator-splitting.” In: *Journal of computational physics* 62.1 (1986), pp. 40–65.
- [91] PK Senecal et al. “Multi-dimensional modeling of direct-injection diesel spray liquid length and flame lift-off length using CFD and parallel detailed chemistry.” In: *SAE transactions* (2003), pp. 1331–1351.
- [92] Stephen R Turns et al. *Introduction to combustion*. Vol. 287. McGraw-Hill Companies New York, NY, USA, 1996.
- [93] 2022. URL: <https://www.openfoam.com/>.
- [94] T J&Poinso and SK Lele. “Boundary conditions for direct simulations of compressible viscous flows.” In: *Journal of computational physics* 101.1 (1992), pp. 104–129.
- [95] Emmanuel Motheau, Ann Almgren, and John B Bell. “Navier–stokes characteristic boundary conditions using ghost cells.” In: *AIAA Journal* 55.10 (2017), pp. 3399–3408.
- [96] Chun Sang Yoo et al. “Characteristic boundary conditions for direct simulations of turbulent counterflow flames.” In: *Combustion Theory and Modelling* 9.4 (2005), pp. 617–646.
- [97] Yu Gong et al. “Numerical investigation of combustion instabilities in swirling flames with hydrogen enrichment.” In: *Flow, Turbulence and Combustion* 111.3 (2023), pp. 953–993.